

# Agnostic Phase Estimation

Xingrui Song,<sup>1</sup> Flavio Salvati,<sup>2</sup> Chandrashekhar Gaikwad,<sup>1</sup> Nicole Yunger Halpern,<sup>3,4</sup> David R. M. Arvidsson-Shukur,<sup>5</sup> and Kater Murch<sup>1</sup>

<sup>1</sup>*Department of Physics, Washington University, St. Louis, Missouri 63130, USA*

<sup>2</sup>*Cavendish Laboratory, Department of Physics, University of Cambridge, Cambridge, CB3 0HE, United Kingdom*

<sup>3</sup>*Joint Center for Quantum Information and Computer Science,*

*NIST and University of Maryland, College Park, Maryland 20742, USA*

<sup>4</sup>*Institute for Physical Science and Technology, University of Maryland, College Park, Maryland 20742, USA*

<sup>5</sup>*Hitachi Cambridge Laboratory, J. J. Thomson Avenue, Cambridge CB3 0HE, United Kingdom*

(Dated: March 4, 2024)

The goal of quantum metrology is to improve measurements' sensitivities by harnessing quantum resources. Metrologists often aim to maximize the quantum Fisher information, which bounds the measurement setup's sensitivity. In studies of fundamental limits on metrology, a paradigmatic setup features a qubit (spin-half system) subject to an unknown rotation. One obtains the maximal quantum Fisher information about the rotation if the spin begins in a state that maximizes the variance of the rotation-inducing operator. If the rotation axis is unknown, however, no optimal single-qubit sensor can be prepared. Inspired by simulations of closed timelike curves, we circumvent this limitation. We obtain the maximum quantum Fisher information about a rotation angle, regardless of the unknown rotation axis. To achieve this result, we initially entangle the probe qubit with an ancilla qubit. Then, we measure the pair in an entangled basis, obtaining more information about the rotation angle than any single-qubit sensor can achieve. We demonstrate this metrological advantage using a two-qubit superconducting quantum processor. Our measurement approach achieves a quantum advantage, outperforming every entanglement-free strategy.

*Introduction.*—Phase estimation is crucial to quantum information processing. Several quantum algorithms use phase estimation as a subroutine for finding unitary operators' eigenvalues [1–6]. Furthermore, phase estimation is used in quantum metrology, the field of using quantum systems to probe, measure, and estimate unknown physical parameters [7–9]. Conventionally, phase estimation requires *a priori* knowledge about the unitary being inferred about.

For example, consider a unitary  $e^{iH}$  generated by a Hamiltonian  $H$ . In quantum algorithms, phase estimation encodes in a qubit register an estimate of an  $e^{iH}$  eigenvalue [10, 11]. To perform this encoding, one must initialize another qubit register in an  $H$  eigenstate. Without information about  $H$ , conventional algorithmic phase estimation fails.

In quantum metrology, phase estimation is often used to infer some unknown parameter  $\alpha$  in a unitary  $U_\alpha = e^{i\alpha A}$ . The Hermitian generator  $A = \sum_i a_i |a_i\rangle\langle a_i|$  has eigenstates  $|a_i\rangle$  and eigenvalues  $a_i$ . Physically,  $\alpha$  could quantify an unknown field's strength. One can estimate  $\alpha$  by applying  $U_\alpha$  to several quantum systems and measuring them. The optimal single-qubit probe states are the equal-weight superpositions of the  $A$  eigenstates associated with the greatest and least eigenvalues, e.g.,  $(|a_{\min}\rangle + |a_{\max}\rangle)/\sqrt{2}$  [7–9]. The optimal measurement observables depend on  $A$ , too. Without information about  $A$ , therefore, conventional metrological phase estimation fails.

If  $H$  or  $A$  is unknown, one can learn about it through quantum-process tomography [12–15], then optimize probes. However, process tomography requires many applications of  $e^{iH}$  or  $U_\alpha$ , plus many measure-

ments. The number of applications of a unitary quantifies resource usage in quantum computing and metrology. Hence tomography is costly. Furthermore, one often cannot rely on process tomography to prepare optimal quantum systems. For example, consider a magnetic field whose direction changes. We might wish to measure the field strength  $\alpha$  at some instant. The probes must be prepared optimally beforehand.

A recent work [16] outlined a phase-estimation protocol for when information about  $A$  becomes available *after* the unitary is applied. The protocol harnesses the mathematical equivalence between certain entanglement-manipulation experiments and closed timelike curves, hypothetical worldlines that travel backward in time [17–22]. In the protocol of [16], one entangles a probe with an ancilla. After information about  $A$  becomes available, one effectively updates the probe's initial state, by measuring the ancilla, using the equivalence. The results in [16] inspire metrological protocols that leverage entanglement to circumvent requirements of *a priori* information. Optics experiments have explored the relationship between entanglement manipulation and closed timelike curves [23, 24]. Additionally, delayed-choice quantum-eraser experiments [25, 26] resemble the protocol in [16] conceptually. However, metrological protocols inspired by closed timelike curves have not been reported, to our knowledge.

In this Letter, we show that entanglement manipulation can enable optimal estimation of  $\alpha$ , even sans information about  $A$ . We consider a common scenario: an arbitrary unbiased estimator  $\hat{\alpha}$  is calculated from  $N$  measurement outcomes. The *Fisher information* (FI)  $I_\alpha$  quantifies the outcome probabilities' sensitivity to small

changes in  $\alpha$ . We define  $I_\alpha$  below; it limits the estimator's variance through the *Cramér–Rao bound*:  $\text{var}(\hat{\alpha}) \geq 1/(NI_\alpha)$ . We theoretically prove that entanglement can boost the FI of  $\alpha$  by 50%. Our protocol is optimal, achieving the FI of the optimal protocol that leverages knowledge of  $A$ . Using a two-qubit superconducting processor, we experimentally demonstrate the advantage.

The rest of this paper is organized as follows. The next four sections present and experimentally demonstrate four strategies for inferring about  $\alpha$  without knowledge of the rotation axis  $\hat{\mathbf{n}}$ . A *single-qubit sensor* can extract no information about  $\alpha$ . Two time-travel-inspired protocols follow: *hindsight sensing* consumes a maximally entangled two-qubit state. The protocol achieves an FI of 1 if information about  $\hat{\mathbf{n}}$  becomes available eventually. *Agnostic sensing* requires a maximally entangled two-qubit state and an entangling measurement. The protocol achieves an FI of 1 even if  $\hat{\mathbf{n}}$  remains unknown. We compare these entanglement-boosted protocols to *entanglement-free sensing with an ancilla*, which achieves an FI of 2/3. The final section clarifies our results' significance and the opportunities they engender.

*Single-qubit quantum sensor.*—We start with the simplest quantum sensor: a qubit probe subject to an arbitrary unknown rotation, represented by the operator  $U_\alpha = \exp(-i\alpha\hat{\mathbf{n}} \cdot \boldsymbol{\sigma}/2)$ . The unknown rotation angle is  $\alpha$ ,  $\hat{\mathbf{n}} = \sin\theta \cos\phi \hat{\mathbf{x}} + \sin\theta \sin\phi \hat{\mathbf{y}} + \cos\theta \hat{\mathbf{z}}$  defines the unknown rotation axis, and  $\boldsymbol{\sigma} = (X, Y, Z)$  denotes a vector of Pauli operators. Figure 1(a) illustrates the protocol: the probe is prepared in  $|\psi\rangle$ , is mapped to  $|\psi_\alpha\rangle := U_\alpha |\psi\rangle$ , and is projectively measured in a chosen basis. The protocol's goal is to infer the rotation angle  $\alpha$ .

Consider measuring the probe in an arbitrary basis  $\{|i\rangle\}$ . Outcome  $i$  occurs with probability  $P_i = |\langle i|\psi_\alpha\rangle|^2$ . The FI quantifies these probabilities'  $\alpha$ -sensitivity:  $I_\alpha = \sum_{i=0,1} \frac{(\partial_\alpha P_i)^2}{P_i}$ . The FI is upper-bounded by the *quantum Fisher information* (QFI),  $\mathcal{I}_\alpha$  [7, 27]:

$$I_\alpha \leq \mathcal{I}_\alpha = 4 \left( \langle \partial_\alpha \psi_\alpha | \partial_\alpha \psi_\alpha \rangle - |\langle \psi_\alpha | \partial_\alpha \psi_\alpha \rangle|^2 \right). \quad (1)$$

The QFI, in turn, is upper-bounded by the maximum variance of the operator  $\hat{\mathbf{n}} \cdot \hat{\boldsymbol{\sigma}}/2$  that generates  $U_\alpha$ :  $\mathcal{I}_\alpha \leq 4 \max_{|\psi\rangle} \{\text{var}(\hat{\mathbf{n}} \cdot \hat{\boldsymbol{\sigma}}/2)\} = 1$ . Consider the limit of many trials (as  $N \rightarrow \infty$ ). If  $\hat{\mathbf{n}}$  is known, all bounds (including the Cramér–Rao bound from the introduction) can be saturated:

$$\text{var}(\hat{\alpha}) = \frac{1}{NI_\alpha} = \frac{1}{N\mathcal{I}_\alpha} = \frac{1}{4N \max_{|\psi\rangle} \{\text{var}(\frac{\hat{\mathbf{n}} \cdot \hat{\boldsymbol{\sigma}}}{2})\}} = \frac{1}{N}. \quad (2)$$

If  $\hat{\mathbf{n}}$  is unknown, neither saturation happens, typically [28].

Figure 1(b) depicts the protocol on the Bloch sphere. The red and blue lines represent possible initial states. Without loss of generality, we choose for the rotation axis to lie in the  $\hat{\mathbf{x}}\text{--}\hat{\mathbf{z}}$ -plane. We choose the pure initial state's Bloch vector to be  $\hat{\boldsymbol{\psi}} = \sin(\lambda)\hat{\mathbf{x}} + \cos(\lambda)\hat{\mathbf{z}}$ , illustrating a range of metrological outcomes, from worst to

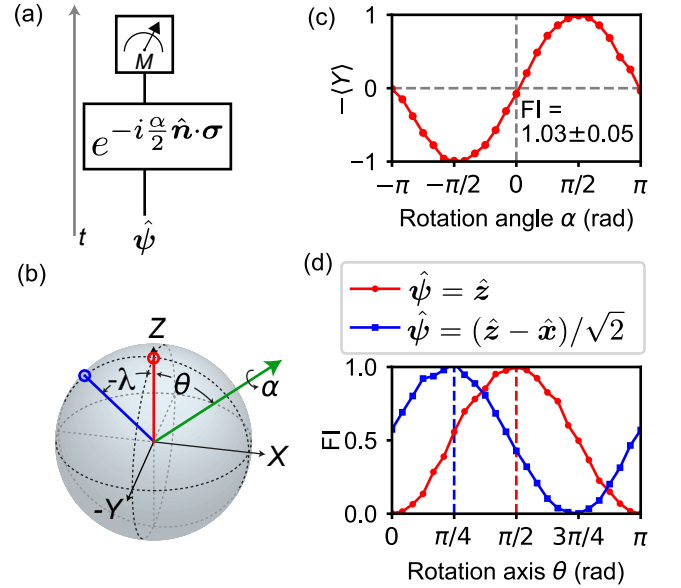


**FIG. 1. Fisher information achievable by a single-qubit sensor.** (a) Protocol for sensing the rotation angle  $\alpha$ . Time runs along the vertical direction, as in the closed time-like-curve representation introduced later. (b) Bloch-sphere representation of the protocol. The red and blue lines represent possible initial states. The green arrow indicates the rotation axis. (c) Outcomes from preparing  $\hat{\boldsymbol{\psi}} = \hat{\mathbf{z}}$ , then rotating about the  $\hat{\mathbf{x}}$ -axis through a varying rotation angle  $\alpha$ . The red points and curve represent the measured  $-\langle Y \rangle$  values, from which we infer the FI ( $\pm$  one standard deviation). (d) FI measured at various rotational axes parameterized by  $\theta$ . If the initial state is  $\hat{\boldsymbol{\psi}} = \hat{\mathbf{z}}$  (red curve), the FI fails to achieve its maximum value, except if  $\theta = \pi/2$  specifies the rotational axis. An analogous statement concerns  $\hat{\boldsymbol{\psi}} = (\hat{\mathbf{z}} - \hat{\mathbf{x}})/\sqrt{2}$  (blue curve) and  $\theta = \pi/4$ .

optimal. Figure 1(b) shows two possible initial states, with  $\lambda = 0$  (red) and  $\lambda = -\pi/4$  (blue). The Supplemental Material [28] details how we implement single-qubit rotations. The rotation leaves the probe in the state  $|\psi_\alpha\rangle$ . Our later analysis governs all  $\alpha \in [-\pi, \pi]$ , but illustrating with infinitesimal rotation angles  $d\alpha$  first is instructive. An infinitesimal rotation displaces the Bloch vector by an amount  $d\boldsymbol{\psi} = \hat{\mathbf{n}} \times \hat{\boldsymbol{\psi}} d\alpha = \sin(\lambda - \theta)\hat{\mathbf{y}} d\alpha = \hat{\mathbf{y}} d\langle Y \rangle$ . Therefore, an optimal final measurement is of  $Y$ .

Figure 1(c) displays data from optimal measurements. We show  $-\langle Y \rangle$  at multiple  $\alpha$  values for the initial state  $\lambda = 0$  and rotation-axis parameter  $\theta = \pi/2$ . We have calibrated and corrected for the  $\approx 98\%$  measurement fidelity throughout this work [28]. Fitting the outcomes to a sinusoid, we infer the  $P_i$ s at  $\alpha = 0$ . From these  $P_i$ s, we calculate  $I_\alpha = 1.03 \pm 0.05$ , a value consistent with the maximum predicted QFI.

Figure 1(d) displays the measured FI for various rotation axes. The red curve (initial state parameterized by  $\lambda = 0$ ) shows that the maximum FI is achieved only when  $\theta = \pi/2$ . The blue curve (initial state parameterized by

$\lambda = -\pi/4$ ) shows a maximum FI only at  $\theta = \pi/4$ . These results illustrate a point stated above: one can generally obtain the maximum possible FI about a rotation  $\alpha$  only if *a priori* knowledge about  $\theta$  informs the probe's preparation and measurement. This limitation betrays a deeper problem with the single-qubit probe, as discussed in [28]:  $U_\alpha$  has three unknown parameters, whereas a qubit has two degrees of freedom (DOFs). Estimating  $\alpha$ , when the rotation axis is unknown, is therefore typically impossible.

*Hindsight sensing.*—Let us relax the requirement of *a priori* knowledge about the rotation axis  $\hat{n}$ . We harness the connection between closed timelike curves and entanglement [29–32]. Consider preparing a maximally entangled (Bell) state [depicted by the symbol  $\cup$  in Fig. 2(a)] between *two* qubits at a time  $T_1$ . One can view this preparation as the chronology-violating trajectory of *one* qubit that travels backward in time, turns around at  $T_1$ , and continues forward in time [19–22]. We harness this connection to effectively choose a probe's initial state *in hindsight*.

Figure 2(a) illustrates this strategy. At  $T_1$ , we initialize a probe qubit and an ancilla qubit in a singlet. A unitary  $U_\alpha$  rotates the probe's state about an unknown axis  $\hat{n}$ . Afterward,  $\hat{n}$  is revealed; Eq. (2) can be satisfied. We measure the ancilla along an axis orthogonal to  $\hat{n}$ . The measurement projects the ancilla onto an optimal rotation-sensing state. The probe's state comes to be orthogonal to the ancilla's. One can imagine that the time-traveling qubit in Fig. 2(a) is flipped at  $T_1$ . Hence we say that our experiment is *inspired* by closed timelike curves.

In previous metrology protocols [33–36], the measurement of an ancilla determined whether the probe would undergo a final, information-acquiring measurement. Our protocol always features measurements of the probe and the ancilla. The ancilla-measurement outcomes help us postprocess the data from probe-measurement outcomes to infer about  $\alpha$ .

Four Bell states exist, and all serve equally well in our protocol, we prove in the Supplemental Material [28]. We illustrate with the singlet state, whose effectiveness one can understand intuitively through the state's rotational invariance:

$$|\Psi^-\rangle = \frac{1}{\sqrt{2}} (|b\rangle_P |\bar{b}\rangle_A - |\bar{b}\rangle_P |b\rangle_A). \quad (3)$$

P denotes the probe; and A, the ancilla. The structure of  $|\Psi^-\rangle$  does not depend on the single-qubit basis  $\{|b\rangle, |\bar{b}\rangle\}$ ;  $|\Psi^-\rangle$  remains invariant under identical rotations of P and A. We denote by  $|a_0\rangle$  and  $|a_1\rangle$  the  $-\hat{n} \cdot \hat{\sigma}/2$  eigenstates associated with the eigenvalues  $+\frac{1}{2}$  and  $-\frac{1}{2}$ . Define the superpositions  $|a^\pm\rangle \equiv (|a_0\rangle \pm |a_1\rangle)/\sqrt{2}$ . If the ancilla's  $\{|a^\pm\rangle\}$  is measured, the probe is projected onto an optimal state for measuring  $\alpha$ .

Figure 2 details this protocol's experimental implementation. Using a parametric entangling gate, we prepare the probe and ancilla in a singlet [28]. We then rotate

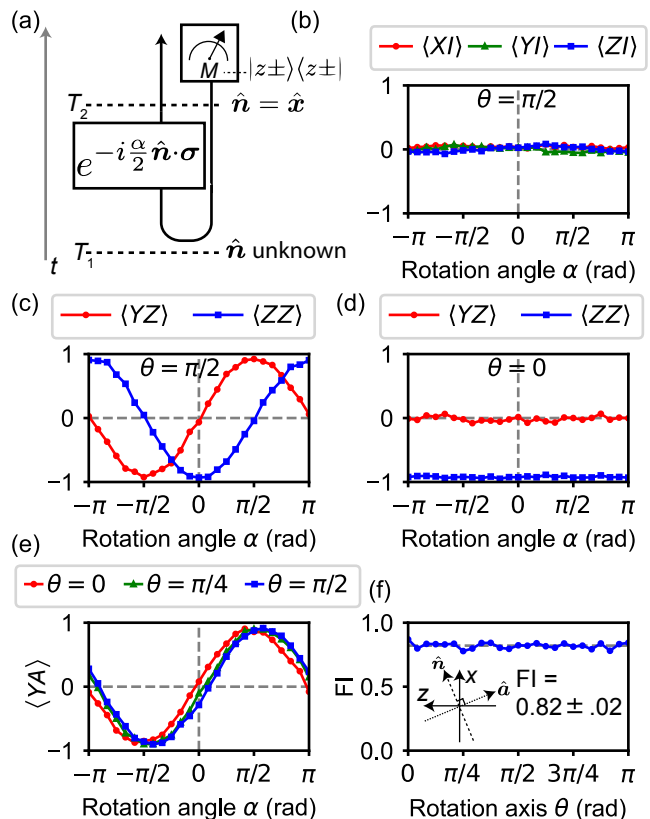


FIG. 2. **Entangled sensor inspired by closed timelike curve.** (a) Protocol for sensing the rotation angle  $\alpha$  by mimicking a closed timelike curve. The ancilla's state effectively travels backward in time. It flips at  $T_1$ , becoming an optimal probe state. (b) The probe has no Pauli operator whose expectation value carries information about  $\alpha$ . (c) If the rotation is about the  $x$ -axis (if  $\theta = \pi/2$ ), the probe–ancilla correlators  $\langle YZ \rangle$  and  $\langle ZZ \rangle$  contain information about  $\alpha$ . (d) However, for different rotations about the  $z$ -axis ( $\theta = 0$ ), the same correlators contain no information about  $\alpha$ . (e) The correlator  $\langle YA \rangle$  depends on the optimal ancilla observable to measure.  $\langle YA \rangle$  is sensitive to the rotational angle  $\alpha$ , at rotation axes parameterized by  $\theta = 0, \pi/4$ , and  $\pi/2$ . (f) From the correlator, we calculate the FI, for various rotational axes. The FI remains close to the optimal value, 1. The subfigure indicates the optimal ancilla measurement axis  $\hat{a}$ .

the probe and perform tomography on the probe–ancilla state. Figure 2(b) displays the probe's Pauli-operator expectation values when  $\theta = \pi/2$  parameterizes the rotation axis. These expectation values encode no information about  $\alpha$ , the flat curves indicate. This lack is expected, since the probe's and ancilla's reduced states are maximally mixed.

To learn about  $\alpha$ , we must calculate two-qubit correlators. Figure 2(c) illustrates with  $\langle YZ \rangle$ . We have used entanglement to reproduce the results of Fig. 1(c): measuring the ancilla's  $Z$  projects the probe's Bloch vector onto  $\pm \hat{z}$ , which are both optimal for sensing  $\alpha$ . However, the sensor's sensitivity depends on the rotation axis.

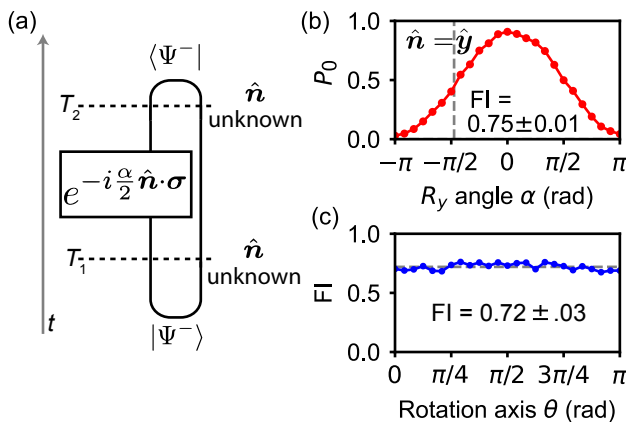


FIG. 3. **Agnostic sensing.** (a) Protocol: The probe and ancilla are prepared in a singlet. The probe is rotated, whereupon we measure whether the qubits are still in the singlet. (b)  $P_0$  denotes the probability of obtaining the *yes* outcome. From  $P_0$ , we infer the FI. Different plots follow from rotations about the  $\hat{x}$ -,  $\hat{y}$ -, and  $\hat{z}$ -axes. (c) FI inferred after various rotations in the  $\hat{x}$ - $\hat{z}$  plane.

$\langle YZ \rangle$  and  $\langle ZZ \rangle$  cannot register rotations about the  $\hat{z}$ -axis ( $\theta = 0$ ), Fig. 2(d) shows.

We interpret these results using the language of closed time-like curves [37]. When the qubits are initialized in a singlet at  $T_1$ , the probe is configured agnostically: for every axis  $\hat{m}$ ,  $\langle \sigma \cdot \hat{m} \rangle = 0$ . The probe is waiting for the optimal-state input from the future. The probe undergoes the rotation; and the ancilla's optimal basis,  $\{|a^\pm\rangle\}$ , is measured at  $T_2$ . The measurement projects the ancilla's state onto  $|a^\pm\rangle$ . This state is effectively sent backward in time and flipped into  $|a^\mp\rangle$ , to serve as the probe's time- $T_1$  state. Thus, the probe is retroactively prepared in the optimal state; is rotated with  $U_\alpha$ ; and, at  $T_2$ , undergoes a  $Y$  measurement.

Figure 2(e) demonstrates that we can obtain the maximum FI by measuring the ancilla in an  $\hat{n}$ -dependent manner, e.g., by measuring  $\{|a^\pm\rangle\}$ . Figure 2(f) displays the FI obtained when  $\theta \in [0, \pi]$  parameterizes the rotation axis. Regardless of the axis, we obtain a QFI of  $\approx 0.82$ . This value is less the maximum possible QFI, due to the finite fidelity of the entangled-state preparation, detailed in [28].

*Agnostic sensing.*—The previous section's protocol allows us to effectively choose the probe's initial state after  $U_\alpha$ . We now show that an entangling measurement, beyond the entangled initial state, enables an optimal sensing strategy that requires neither *a priori* nor *a posteriori* knowledge of the rotation axis: what we term an *agnostic sensor*.

Figure 3(a) sketches the protocol. As before, we initialize the probe and ancilla in a singlet,  $|\Psi^-\rangle$ . Then, the probe undergoes an unknown rotation  $U_\alpha$ . The unitary

maps  $|\Psi^-\rangle$  to

$$|\Psi_\alpha^-\rangle = \frac{1}{\sqrt{2}} \left( e^{+i\frac{\alpha}{2}} |a_0\rangle_P |a_1\rangle_A + e^{-i\frac{\alpha}{2}} |a_1\rangle_P |a_0\rangle_A \right). \quad (4)$$

Finally, we perform an entangling measurement of  $\{\Pi_0 := |\Psi^-\rangle\langle\Psi^-|, \Pi_1 := \mathbb{1} - \Pi_0\}$ . The possible outcomes' probabilities are

$$P_0 := |\langle\Psi_\alpha^-|\Pi_0|\Psi_\alpha^-\rangle|^2 = \cos^2(\alpha/2) \quad \text{and} \quad (5)$$

$$P_1 := |\langle\Psi_\alpha^-|\Pi_1|\Psi_\alpha^-\rangle|^2 = \sin^2(\alpha/2). \quad (6)$$

This strategy produces the maximum FI about  $\alpha$ , regardless of the rotation axis [7]. More broadly, Eq. (2) holds.

We can understand this result through closed timelike curves. If  $\alpha = 0$ , then  $U_\alpha$  does not perturb the initial state  $|\Psi^-\rangle$ , and  $P_0 = 1$ . The ancilla-probe pair maps onto a particle traversing a closed timelike curve infinitely many times [21, 22]. If  $\alpha \neq 0$ , the particle interacts with the field that imprints  $\alpha$  on the state. Consequently, the experiment has a probability  $P_0 < 1$  of successfully simulating a closed timelike curve. Knowing this success probability enables us to estimate  $\alpha$ .

Figure 3 details our experimental demonstration of agnostic sensing. We prepare the singlet via an  $\sqrt{i}$ SWAP gate [28]. The probe then undergoes  $U_\alpha$ . Finally, we measure  $\{\Pi_0, \Pi_1\}$  by rotating the ancilla, performing another  $\sqrt{i}$ SWAP, (this process maps the singlet onto separable states) and measuring the probe's and ancilla's  $Z$  eigenbases. From many trials' outcomes, we infer  $P_0$ .

We measure  $P_0$  for rotations about the  $\hat{x}$ -,  $\hat{y}$ -, and  $\hat{z}$ -axes, for several  $\alpha$  values [Fig. 3(b-d)]. As expected,  $P_0 \propto \cos^2(\alpha/2)$ , independently of the rotation axis. We fit  $P_0$  near  $\alpha = -\pi/2$  to infer the FI. Figure 3(e) displays the measured FI for rotation axes  $\theta \in [0, \pi]$ : regardless of the axis,  $\mathcal{I}_\alpha = 0.72$ .

The two-qubit gate's fidelity limits the FI here, as in the previous protocol. This protocol requires two such gates, so the infidelity impacts the FI more. This proportionality highlights a potential trade-off between quantum advantage and circuit depth.

*Entanglement-free sensing with ancilla.*—To highlight our agnostic sensor's quantum advantage, we compare it with an optimal entanglement-free sensor. Imagine restricting the probes to identical single-qubit pure states. All pure states serve equally well for sensing  $\alpha$ , by symmetry: the rotation axis is unknown. Without loss of generality, therefore, we suppose that the probes begin in  $|\psi\rangle = |0\rangle$ . Three independent, unknown parameters specify  $U_\alpha$ : the rotation angle  $\alpha$ , as well as the rotation axis's zenith angle  $\theta$  and azimuthal angle  $\phi$ . We cannot estimate 3 parameters using a qubit, whose state encodes only 2 DOFs. For every single-qubit probe, there exist  $(\alpha, \theta, \phi)$  values for which  $\mathcal{I}_\alpha = 0$ . Hence, no single-qubit probes achieve Eq. (2), we prove in [28].

Nevertheless, one can estimate  $\alpha$  without consuming entanglement, e.g., by performing quantum process tomography on  $U_\alpha$  [39, 40]. Since  $\hat{n}$  is unknown, the most



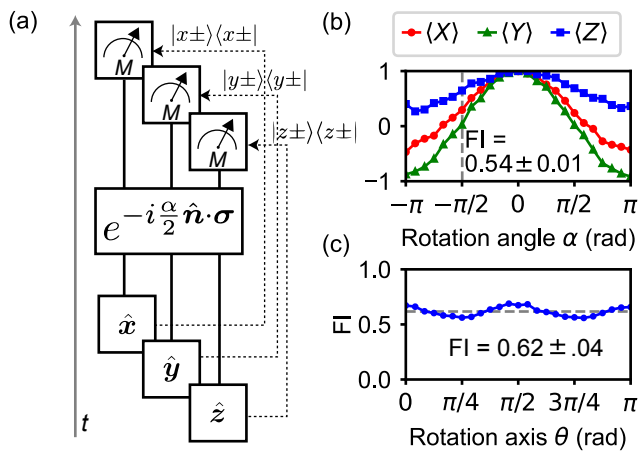


FIG. 4. **Entanglement-free sensing with ancilla** (a) Protocol: Single-qubit-probe states are tagged with classical ancillas that determine the final-measurement basis (dashed lines). (b) For a rotation about the  $(\theta = \pi/5, \phi = \pi/9)$  axis, different single-qubit-probe states yield different FI values. (c) FI values inferred after various rotations [38].

reasonable prior distribution for  $\hat{\mathbf{n}}$  is uniform. We describe a strategy for garnering the greatest average FI inferable from any entanglement-free input: prepare the qubit probe in a state  $|\psi_j\rangle$ , tagged with an ancilla state  $|j\rangle$ , with probability  $p_j$ :

$$\rho_0 = \sum_j p_j |\psi_j\rangle\langle\psi_j| \otimes |j\rangle\langle j|, \text{ wherein } \sum_j p_j = 1. \quad (7)$$

We show the following in [28]. First, for all  $\rho_0$ , the QFI about  $\alpha$ , averaged over the  $\hat{\mathbf{n}}$ , equals  $2/3$ . Second, not all  $\rho_0$  achieve the first two equalities in Eq. (2). Third, we derive the form of the states  $\rho_0$  for which (i)  $\mathcal{I}_\alpha = 2/3$  independently of  $\hat{\mathbf{n}}$  and (ii) the first two equalities in Eq. (2) hold. Examples include  $\rho_\star = (|x+\rangle\langle x+| \otimes |1\rangle\langle 1| + |y+\rangle\langle y+| \otimes |2\rangle\langle 2| + |z+\rangle\langle z+| \otimes |3\rangle\langle 3|)/3$ , where  $|x+\rangle$  denotes the eigenvalue-1  $X$  eigenstate, etc. Preparing and optimally measuring  $\rho_\star$  yields a FI of  $2/3$  about  $\alpha$  [Eq. (B33)], irrespectively of  $\hat{\mathbf{n}}$ .

Figure 4 displays our experimental implementation of this entanglement-free strategy. We prepare  $\rho_\star$ . If the probe is in  $|x+\rangle$ , the optimal measurement is of  $X$ ; if  $|y+\rangle$ , then  $Y$ ; and, if  $|z+\rangle$ , then  $Z$ . We use the ancilla as a record of the initial probe state, to choose the optimal measurement.

In this scenario, we can calculate the QFI by averaging the QFI values obtained from the probabilistically combined input states [28]:  $\mathcal{I}_\alpha = I_\alpha = \frac{1}{3}(\mathcal{I}_{\alpha,|x+} + \mathcal{I}_{\alpha,|y+} + \mathcal{I}_{\alpha,|z+}) = 2/3$ . We measure the FI for different rotation axes, as when demonstrating the previous sensing protocols. We achieve an average axis-independent FI of  $0.62$ , consistently with the theoretical maximum of  $2/3$ .

*Discussion.*—In the seminal review [41], the authors distinguish a hierarchy of quantum sensors: those which leverage energy-level quantization (type I), those which

leverage quantum coherence (type II), and those which leverage entanglement (type III). We have introduced a type-III sensor. It achieves an advantage over the more-classical type-II sensors. The 50 % improvement in the QFI weighs against the cost of entanglement manipulation. One cost that we avoid is postselection: we discard no data. All measurement outcomes inform our inference of  $\alpha$ , despite a known relationship between postselection and closed timelike curves [29, 30].

One can extend our hindsight and agnostic protocols to improve our quantum sensors. As described above, we applied  $U_\alpha$  to each probe once before measuring the probe. Denote by  $\nu$  the total number of applications of  $U_\alpha$  in all trials, and denote by  $\hat{\alpha}$  any unbiased estimator of  $\alpha$ . The estimator’s variance scales as  $\delta\hat{\alpha} \sim 1/\nu$  in the large- $\nu$  limit, by the Cramér–Rao bound. Instead, we can apply  $U_\alpha$  to a probe multiple times before measuring the probe. This strategy can achieve Heisenberg scaling, the optimal scaling of  $\delta\hat{\alpha}$  when  $U_\alpha$  applications form the costly resource:  $\delta\hat{\alpha} \sim 1/\nu^2$  [8, 9, 42–44]. The states usable to achieve Heisenberg scaling include those prepared in our hindsight and agnostic protocols [44].

Several avenues for future research suggest themselves. First, our protocol merits extending to optical and solid-state systems that have concrete metrological applications. Second, our protocol may benefit phase estimation in quantum algorithms. Third, our experiment was inspired by the theoretical application of closed timelike curves to metrology [16]. More precisely, the application was to weak-value amplification, a technique for sensing interaction strengths [45–51]. One can experimentally implement the application to weak-value amplification or to a more general technique, partially postselected amplification [35]. Fourth, we expect our technique to be useful in metrology subject to time constraints. For example, one may need to measure a time-varying field at a certain instant [52–54]. To date, optimal sensing strategies have required *a priori* knowledge about the unknown unitary’s generator,  $A$ . Our agnostic protocol entails optimal state preparations and measurements without this knowledge.

## ACKNOWLEDGMENTS

*Acknowledgments.*—The authors are thankful for discussions with Aephraim Steinberg and his lab. This research was supported in part by grant NSF PHY-2309135 to the Kavli Institute for Theoretical Physics (KITP). This project was initiated at the KITP program “New directions in quantum metrology.” This research was further supported by NSF Grant PHY-2309135 to the Kavli Institute for Theoretical Physics (KITP), PHY-1752844 (CAREER), NSF QLCI grant OMA-2120757, the Air Force Office of Scientific Research (AFOSR) Multidisciplinary University Research Initiative (MURI) Award on Programmable systems with non-Hermitian quantum dynamics (Grant No. FA9550-21-1-0202), ONR Grant

No. N00014- 21-1-2630, and by the Gordon and Betty Moore Foundation, grant DOI 10.37807/gbmf11557. The device was fabricated and provided by the Superconducting Qubits at Lincoln Laboratory (SQUILL) Foundry at MIT Lincoln Laboratory, with funding from the Labo-

ratory for Physical Sciences (LPS) Qubit Collaboratory. D.R.M.A.S. acknowledges support from Girton College, Cambridge. F.S. was supported by the Harding Foundation.

- 
- [1] P. Shor, Algorithms for quantum computation: discrete logarithms and factoring, in *Proc. of the 35th FOCS* (IEEE, New York, 1994) pp. 124–134.
- [2] G. Brassard, P. Hoyer, M. Mosca, and A. Tapp, Quantum amplitude amplification and estimation, *Contemporary Mathematics* **305**, 53 (2002).
- [3] B. Bauer, S. Bravyi, M. Motta, and G. K.-L. Chan, Quantum algorithms for quantum chemistry and quantum materials science, *Chem. Rev.* **120**, 12685 (2020).
- [4] Y. Suzuki, S. Uno, R. Raymond, T. Tanaka, T. Onodera, and N. Yamamoto, Amplitude estimation without phase estimation, *Quantum Inf. Process.* **19**, 1 (2020).
- [5] S. Lloyd, S. Bosch, G. D. Palma, B. Kiani, Z.-W. Liu, M. Marvian, P. Reberntrost, and D. M. Arvidsson-Shukur, Quantum polar decomposition algorithm (2020), arXiv:2006.00841.
- [6] S. Lloyd, B. T. Kiani, D. R. M. Arvidsson-Shukur, S. Bosch, G. D. Palma, W. M. Kaminsky, Z.-W. Liu, and M. Marvian, Hamiltonian singular value transformation and inverse block encoding (2021), arXiv:2104.01410.
- [7] S. L. Braunstein and C. M. Caves, Statistical distance and the geometry of quantum states, *Phys. Rev. Lett.* **72**, 3439 (1994).
- [8] V. Giovannetti, S. Lloyd, and L. Maccone, Quantum metrology, *Physical review letters* **96**, 010401 (2006).
- [9] V. Giovannetti, S. Lloyd, and L. Maccone, Advances in quantum metrology, *Nature photonics* **5**, 222 (2011).
- [10] A. Y. Kitaev, (1995), arXiv:quant-ph/9511026.
- [11] M. A. Nielsen and I. L. Chuang, *Quantum Computation and Quantum Information: 10th Anniversary Edition*, 10th ed. (Cambridge University Press, New York, NY, USA, 2011).
- [12] I. L. Chuang and M. A. Nielsen, Prescription for experimental determination of the dynamics of a quantum black box, *Journal of Modern Optics* **44**, 2455 (1997), <https://www.tandfonline.com/doi/pdf/10.1080/09500349708231894>.
- [13] G. M. D’Ariano and P. Lo Presti, Quantum tomography for measuring experimentally the matrix elements of an arbitrary quantum operation, *Phys. Rev. Lett.* **86**, 4195 (2001).
- [14] J. B. Altepeter, D. Branning, E. Jeffrey, T. C. Wei, P. G. Kwiat, R. T. Thew, J. L. O’Brien, M. A. Nielsen, and A. G. White, Ancilla-assisted quantum process tomography, *Phys. Rev. Lett.* **90**, 193601 (2003).
- [15] X. Song, M. Naghiloo, and K. Murch, Quantum process inference for a single-qubit maxwell demon, *Physical Review A* **104**, 10.1103/physreva.104.022211 (2021).
- [16] D. R. M. Arvidsson-Shukur, A. G. McConnell, and N. Yunger Halpern, Nonclassical advantage in metrology established via quantum simulations of hypothetical closed timelike curves, *Phys. Rev. Lett.* **131**, 150202 (2023).
- [17] K. Gödel, An example of a new type of cosmological solutions of einstein’s field equations of gravitation, *Rev. Mod. Phys.* **21**, 447 (1949).
- [18] M. S. Morris, K. S. Thorne, and U. Yurtsever, Wormholes, time machines, and the weak energy condition, *Phys. Rev. Lett.* **61**, 1446 (1988).
- [19] C. H. Bennett, in *Proceedings of QUPON* (Wien, 2005).
- [20] G. Svetlichny, Time travel: Deutsch vs. teleportation, *International Journal of Theoretical Physics* **50**, 3903 (2011).
- [21] S. Lloyd, L. Maccone, R. Garcia-Patron, V. Giovannetti, Y. Shikano, S. Pirandola, L. A. Rozema, A. Darabi, Y. Soudagar, L. K. Shalm, *et al.*, Closed timelike curves via postselection: theory and experimental test of consistency, *Physical Review Letters* **106**, 040403 (2011).
- [22] S. Lloyd, L. Maccone, R. Garcia-Patron, V. Giovannetti, and Y. Shikano, Quantum mechanics of time travel through post-selected teleportation, *Phys. Rev. D* **84**, 025007 (2011).
- [23] M. Ringbauer, M. A. Broome, C. R. Myers, A. G. White, and T. C. Ralph, Experimental simulation of closed timelike curves, *Nature Communications* **5**, 10.1038/ncomms5145 (2014).
- [24] C. Marletto, V. Vedral, S. Virzi, E. Rebufello, A. Avella, F. Piacentini, M. Gramegna, I. P. Degiovanni, and M. Genovese, Theoretical description and experimental simulation of quantum entanglement near open time-like curves via pseudo-density operators, *Nature Communications* **10**, 10.1038/s41467-018-08100-1 (2019).
- [25] F. Kaiser, T. Coudreau, P. Milman, D. B. Ostrowsky, and S. Tanzilli, Entanglement-enabled delayed-choice experiment, *Science* **338**, 637–640 (2012).
- [26] J.-C. Lee, H.-T. Lim, K.-H. Hong, Y.-C. Jeong, M. S. Kim, and Y.-H. Kim, Experimental demonstration of delayed-choice decoherence suppression, *Nature Communications* **5**, 10.1038/ncomms5522 (2014).
- [27] C. W. Helstrom, *Quantum Detection and Estimation Theory*, Vol. 123 (Elsevier, 1976) 1st Edition.
- [28] Supplemental Material contains experimental details, data processing techniques, and further theoretical analysis of the sensing protocols.
- [29] S. Lloyd, L. Maccone, R. Garcia-Patron, V. Giovannetti, Y. Shikano, S. Pirandola, L. A. Rozema, A. Darabi, Y. Soudagar, L. K. Shalm, and A. M. Steinberg, Closed timelike curves via postselection: Theory and experimental test of consistency,

- Physical Review Letters **106**, 10.1103/physrevlett.106.040403 (2011).
- [30] S. Lloyd, L. Maccone, R. Garcia-Patron, V. Giovannetti, and Y. Shikano, Quantum mechanics of time travel through post-selected teleportation, *Phys. Rev. D* **84**, 025007 (2011).
- [31] T. A. Brun and M. M. Wilde, Simulations of closed timelike curves, *Foundations of Physics* **47**, 375 (2017).
- [32] J.-M. A. Allen, Treating time travel quantum mechanically, *Phys. Rev. A* **90**, 042107 (2014).
- [33] D. R. M. Arvidsson-Shukur, N. Yunger Halpern, H. V. Lepage, A. A. Lasek, C. H. W. Barnes, and S. Lloyd, Quantum advantage in postselected metrology, *Nature Communications* **11**, 3775 (2020).
- [34] J. H. Jenne and D. R. M. Arvidsson-Shukur, Unbounded and lossless compression of multiparameter quantum information, *Phys. Rev. A* **106**, 042404 (2022).
- [35] N. Lupu-Gladstein, Y. B. Yilmaz, D. R. M. Arvidsson-Shukur, A. Brodutch, A. O. T. Pang, A. M. Steinberg, and N. Y. Halpern, Negative quasiprobabilities enhance phase estimation in quantum-optics experiment, *Phys. Rev. Lett.* **128**, 220504 (2022).
- [36] F. Salvati, W. Salmon, C. H. W. Barnes, and D. R. M. Arvidsson-Shukur, Compression of metrological quantum information in the presence of noise, arXiv e-prints, arXiv:2307.08648 (2023), arXiv:2307.08648 [quant-ph].
- [37] To clarify, we do not precisely simulate a (postselected) closed timelike curve [29]: we do not discard information through postselection. However, such curves motivate and provide intuition about our experiment [16].
- [38] The FI's weak sinusoidal variation results from experimental imperfections.
- [39] G. M. D'Ariano and P. Lo Presti, Quantum tomography for measuring experimentally the matrix elements of an arbitrary quantum operation, *Phys. Rev. Lett.* **86**, 4195 (2001).
- [40] J. B. Altepeter, D. Branning, E. Jeffrey, T. C. Wei, P. G. Kwiat, R. T. Thew, J. L. O'Brien, M. A. Nielsen, and A. G. White, Ancilla-assisted quantum process tomography, *Phys. Rev. Lett.* **90**, 193601 (2003).
- [41] C. L. Degen, F. Reinhard, and P. Cappellaro, Quantum sensing, *Rev. Mod. Phys.* **89**, 035002 (2017).
- [42] T. Rudolph and L. Grover, Quantum communication complexity of establishing a shared reference frame, *Phys. Rev. Lett.* **91**, 217905 (2003).
- [43] J. G. Smith, C. H. W. Barnes, and D. R. M. Arvidsson-Shukur, Iterative quantum-phase-estimation protocol for shallow circuits, *Phys. Rev. A* **106**, 062615 (2022).
- [44] J. G. Smith, C. H. W. Barnes, and D. R. M. Arvidsson-Shukur, An adaptive bayesian quantum algorithm for phase estimation (2023), arXiv:2303.01517 [quant-ph].
- [45] J. Dressel, M. Malik, F. M. Miatto, A. N. Jordan, and R. W. Boyd, Colloquium: Understanding quantum weak values: Basics and applications, *Rev. Mod. Phys.* **86**, 307 (2014).
- [46] J. Harris, R. W. Boyd, and J. S. Lundeen, Weak value amplification can outperform conventional measurement in the presence of detector saturation, *Phys. Rev. Lett.* **118**, 070802 (2017).
- [47] S. Pang, J. Dressel, and T. A. Brun, Entanglement-assisted weak value amplification, *Phys. Rev. Lett.* **113**, 030401 (2014).
- [48] L. Xu, Z. Liu, A. Datta, G. C. Knee, J. S. Lundeen, Y.-q. Lu, and L. Zhang, Approaching quantum-limited metrology with imperfect detectors by using weak-value amplification, *Phys. Rev. Lett.* **125**, 080501 (2020).
- [49] Y. Aharonov, D. Z. Albert, and L. Vaidman, How the result of a measurement of a component of the spin of a spin-1/2 particle can turn out to be 100, *Phys. Rev. Lett.* **60**, 1351 (1988).
- [50] I. M. Duck, P. M. Stevenson, and E. C. G. Sudarshan, The sense in which a "weak measurement" of a spin-1/2 particle's spin component yields a value 100, *Phys. Rev. D* **40**, 2112 (1989).
- [51] O. Hosten and P. Kwiat, Observation of the spin hall effect of light via weak measurements, *Science* **319**, 787 (2008), <https://www.science.org/doi/pdf/10.1126/science.1152697>.
- [52] W. Tang, F. Lyu, D. Wang, and H. Pan, A new design of a single-device 3d hall sensor: Cross-shaped 3d hall sensor, *Sensors* **18** (2018).
- [53] S. Wei, X. Liao, H. Zhang, J. Pang, and Y. Zhou, Recent progress of fluxgate magnetic sensors: Basic research and application, *Sensors* **21**, 10.3390/s21041500 (2021).
- [54] V. Stankevič, S. Keršulis, J. Dilys, V. Bleizgys, M. Viliūnas, V. Vertelis, A. Maneikis, V. Rudokas, V. Plausinaitienė, and N. Žurauskienė, Measurement system for short-pulsed magnetic fields, *Sensors* **23**, 10.3390/s23031435 (2023).
- [55] C. Gaikwad, D. Kowsari, C. Brame, X. Song, H. Zhang, M. Esposito, A. Ranadive, G. Cappelli, N. Roch, E. M. Levenson-Falk, and K. W. Murch, Entanglement assisted probe of the non-markovian to markovian transition in open quantum system dynamics (2024), arXiv:2401.13735.
- [56] M. Boissonneault, J. M. Gambetta, and A. Blais, Dispersive regime of circuit qed: Photon-dependent qubit dephasing and relaxation rates, *Physical Review A* **79**, 10.1103/physreva.79.013819 (2009).
- [57] T. Walter, P. Kurpiers, S. Gasparinetti, P. Magnard, A. Potocnik, Y. Salathé, M. Pechal, M. Mondal, M. Oppliger, C. Eichler, and A. Wallraff, Rapid high-fidelity single-shot dispersive readout of superconducting qubits, *Physical Review Applied* **7**, 10.1103/physrevapplied.7.054020 (2017).
- [58] A. Ranadive, M. Esposito, L. Planat, E. Bonet, C. Naud, O. Buisson, W. Guichard, and N. Roch, Kerr reversal in josephson meta-material and traveling wave parametric amplification, *Nature Communications* **13**, 1737 (2022).
- [59] J. Rapin and O. Teytaud, Nevergrad - A gradient-free optimization platform, <https://GitHub.com/FacebookResearch/Nevergrad> (2018).
- [60] F. Pedregosa, G. Varoquaux, A. Gramfort, V. Michel, B. Thirion, O. Grisel, M. Blondel, P. Prettenhofer, R. Weiss, V. Dubourg, J. Vanderplas, A. Passos, D. Cournapeau, M. Brucher, M. Perrot, and E. Duchesnay, Scikit-learn: Machine learning in Python, *Journal of Machine Learning Research* **12**, 2825 (2011).
- [61] B. Nachman, M. Urbanek, W. A. de Jong, and C. W. Bauer, Unfolding quantum computer readout noise, *npj Quantum Information* **6**, 10.1038/s41534-020-00309-7 (2020).

- [62] M. Werninghaus, D. J. Egger, F. Roy, S. Machnes, F. K. Wilhelm, and S. Filipp, Leakage reduction in fast superconducting qubit gates via optimal control, *npj Quantum Information* **7**, 10.1038/s41534-020-00346-2 (2021).
- [63] S. Kundu, N. Gheeraert, S. Hazra, T. Roy, K. V. Salunkhe, M. P. Patankar, and R. Vijay, Multiplexed readout of four qubits in 3D circuit QED architecture using a broadband Josephson parametric amplifier, *Applied Physics Letters* **114**, 172601 (2019), [https://pubs.aip.org/aip/apl/article-pdf/doi/10.1063/1.5089729/14524953/172601\\_1\\_online.pdf](https://pubs.aip.org/aip/apl/article-pdf/doi/10.1063/1.5089729/14524953/172601_1_online.pdf).
- [64] D. F. V. James, P. G. Kwiat, W. J. Munro, and A. G. White, Measurement of qubits, *Physical Review A* **64**, 10.1103/physreva.64.052312 (2001).
- [65] M. A. Nielsen and I. L. Chuang, *Quantum Computation and Quantum Information: 10th Anniversary Edition* (Cambridge University Press, 2012).
- [66] M. G. A. Paris, Quantum estimation for quantum technology, *Int. J. Quantum Inf.* **7**, 125 (2009).
- [67] V. Giovannetti, S. Lloyd, and L. Maccone, Advances in quantum metrology, *Nat. Photon.* **5**, 222 (2011).
- [68] V. Giovannetti, S. Lloyd, and L. Maccone, Quantum metrology, *Phys. Rev. Lett.* **96**, 010401 (2006).
- [69] H. Cramer, *Mathematical Methods of Statistics* (Princeton University Press, 1999).
- [70] C. R. Rao, Information and the accuracy attainable in the estimation of statistical parameters, in *Breakthroughs in Statistics: Foundations and Basic Theory*, edited by S. Kotz and N. L. Johnson (Springer, New York, NY, 1992, 1992) pp. 235–247.
- [71] S. L. Braunstein and C. M. Caves, Statistical distance and the geometry of quantum states, *Phys. Rev. Lett.* **72**, 3439 (1994).
- [72] A. Fujiwara and H. Nagaoka, Quantum Fisher metric and estimation for pure state models, *Phys. Lett. A* **201**, 119 (1995).
- [73] J. Liu, H. Yuan, X. Lu, and X. Wang, Quantum Fisher information matrix and multiparameter estimation, *J. Phys. A Math.* **53**, 023001 (2019).
- [74] C. W. Helstrom, Quantum detection and estimation theory, *J. Stat. Phys.* **1**, 231 (1969).
- [75] H. Zhu, Information complementarity: A new paradigm for decoding quantum incompatibility, *Scientific Reports* **5**, 14317 (2015).
- [76] T. Heinosaari, T. Miyadera, and M. Ziman, An invitation to quantum incompatibility, *Journal of Physics A: Mathematical and Theoretical* **49**, 123001 (2016).
- [77] S. Ragy, M. Jarzyna, and R. Demkowicz-Dobrzański, Compatibility in multiparameter quantum metrology, *Physical Review A* **94**, 052108 (2016).
- [78] F. Albarelli, M. Barbieri, M. Genoni, and I. Gianani, A perspective on multiparameter quantum metrology: From theoretical tools to applications in quantum imaging, *Phys. Lett. A* **384**, 126311 (2020).
- [79] A. Z. Goldberg, L. L. Sánchez-Soto, and H. Ferretti, Intrinsic sensitivity limits for multiparameter quantum metrology, *Phys. Rev. Lett.* **127**, 110501 (2021).
- [80] A. Fujiwara, Quantum channel identification problem, *Phys. Rev. A* **63**, 042304 (2001).
- [81] S. Pang, J. Dressel, and T. A. Brun, Entanglement-assisted weak value amplification, *Phys. Rev. Lett.* **113**, 030401 (2014).
- [82] S. Pang and T. A. Brun, Improving the precision of weak measurements by postselection measurement, *Phys. Rev. Lett.* **115**, 120401 (2015).
- [83] S. Alipour and A. T. Rezakhani, Extended convexity of quantum fisher information in quantum metrology, *Phys. Rev. A* **91**, 042104 (2015).
- [84] W. Salmon, F. Salvati, C. K. Long, J. Smith, and D. R. M. Arvidsson-Shukur, Comment on: Extended convexity of quantum fisher information in quantum metrology (2024), paper in preparation.
- [85] J. Gallier, Notes on the schur complement (2010).



## Supplemental Information for “Agnostic Phase Estimation”

### A. EXPERIMENTAL SETUP

The experimental measurements were made within a two-qubit subsection of a three-qubit device. Further details about the overall setup at the hardware level appear in [55]. Figure 5(a) displays a simplified schematic of the relevant portion of the device. There are two transmon circuits; one is fixed-frequency, and one is frequency-tunable via a fast flux line (FFL). This tunability allows us to activate parametric entangling gates by modulating the ancilla’s frequency [Fig. 5(b)]. In this appendix, we sometimes refer to a transmon circuit’s higher-energy eigenstates. We label the energy eigenstates as  $|g\rangle$ ,  $|e\rangle$ , and  $|f\rangle$ ; and we refer to the circuits as qubits when only the two lowest levels are relevant. The two qubits are coupled via an off-resonant bus resonator. Single-qubit rotations are applied via independent drive lines. The qubits are also coupled to separate readout resonators, which are probed by a common feedline.

#### 1. Dispersive readout

The probe and ancilla qubits are dispersively coupled to their respective readout resonators [56], allowing for simultaneous high-fidelity single-shot readout [57]. We employ a heterodyne readout scheme: we multiplex the readout signal by simultaneously sending in two pulses that have different frequencies. We separate the two readouts in the frequency domain for processing. For low-noise amplification, we use a traveling-wave parametric amplifier based on the SNAIL (Superconducting Nonlinear Asymmetric Inductive elements) architecture [58]. The readout fidelity is limited primarily by the narrow cavity bandwidths ( $\kappa$ , as given in Table I), requiring long integration times. We apply  $\pi$ -pulses in the  $\{|e\rangle, |f\rangle\}$ -submanifold to increase the signal-to-noise ratio. We optimize over readout amplitude, frequency, and amplifier-bias settings with a gradient-free optimization algorithm [59]. We determine the multicomponent-pulse-integration envelopes via linear-discriminant analysis and principal-component analysis. Ultimately, we achieve readout fidelities of 98.9 % for the ancilla and 97.8 % for the probe, utilizing a random forest classifier [60]. After this calibration, all tomography results are corrected for these finite readout fidelities [Fig. 5(c)] via the iterative Bayesian-update correction method [61]. The high-fidelity readout is utilized to implement an active reset protocol for the initial state preparation.

#### 2. Single-qubit rotations

In this project, we use four types of single-qubit rotations:

- Single-qubit  $\pi/2$  rotations: The  $\pi/2$  rotations applied about the  $\hat{x}$ - and  $\hat{y}$ -axes are used in quantum state tomography and in the arbitrary-axis rotations detailed below. The  $\pi/2$  rotations last for 72 ns (for the ancilla) and 36 ns (for the probe). The pulse envelopes are obtained from the convolution of a square wave and two cosine-DRAG-style spectrum filters [62]. (DRAG stands for *derivative removal by adiabatic gate*.) We have tuned the two cosine-DRAG-style filters to minimize crosstalk between the two qubits, in addition to minimizing coupling out of the qubit manifolds. The spectral leakage from all the sidelobes is minimized via numerical optimization. We estimate these gates’ fidelity to be 99.6 %.
- Single-qubit  $\pi$  rotations: These are implemented in the same manner as the  $\pi/2$  rotations. However, the pulse durations are 120 ns (for the ancilla) and 64 ns (for the probe).
- The  $\{|e\rangle, |f\rangle\}$  rotations are implemented in the same manner as the  $\{|g\rangle, |e\rangle\}$  rotations, described in the previous two bullet points. The  $\pi/2$ -gate times are 64 ns (for the ancilla) and 36 ns (for the probe). The  $\pi$ -gate times are 100 ns (for the ancilla) and 64 ns (for the probe).
- Single-qubit arbitrary-axis, arbitrary-angle rotations: We represent such a rotation with Euler angles:  $(\theta_U, \phi_U, \lambda_U)$ . The corresponding unitary operator is expressed, relative to the  $Z$  eigenbasis, as

$$U(\theta_U, \phi_U, \lambda_U) = \begin{pmatrix} \cos\left(\frac{\theta_U}{2}\right) & -e^{i\lambda_U} \sin\left(\frac{\theta_U}{2}\right) \\ e^{i\phi_U} \sin\left(\frac{\theta_U}{2}\right) & e^{i(\phi_U + \lambda_U)} \cos\left(\frac{\theta_U}{2}\right) \end{pmatrix}. \quad (\text{A1})$$

	$\omega_q/2\pi$ (GHz)	$ \alpha /2\pi$ (MHz)	$\chi_{qc}/2\pi$ (kHz)	$\omega_c/2\pi$ (GHz)	$\kappa/2\pi$ (kHz)	$T_1$ ( $\mu$ s)	$T_2^*$ ( $\mu$ s)
Ancilla qubit	4.2	212	230	6.94	270	32	41
Probe qubit	4.65	180	250	7.09	206	31	39

TABLE I. Measured parameters of the device used in the experiment.

We realize this unitary (up to a global phase) by a combination of rotations,

$$U(\theta_U, \phi_U, \lambda_U) = R\left(\frac{\pi}{2}, \phi_U - \pi\right) R\left(\frac{\pi}{2}, \theta_U + \phi_U\right) R_z(\theta_U + \phi_U + \lambda_U), \quad (\text{A2})$$

where  $R(\frac{\pi}{2}, \phi)$  is defined as a  $\pi/2$  rotation about the  $(\cos \phi \hat{x} + \sin \phi \hat{y})$  axis. A general  $R(\alpha, \phi)$ , for an arbitrary angle  $\alpha$ , is expressed as

$$R(\alpha, \phi) = \begin{pmatrix} \cos \frac{\alpha}{2} & -ie^{-i\phi} \sin \frac{\alpha}{2} \\ -ie^{i\phi} \sin \frac{\alpha}{2} & \cos \frac{\alpha}{2} \end{pmatrix}. \quad (\text{A3})$$

We implement  $R_z(\alpha)$  (a rotation about the  $\hat{z}$ -axis through an arbitrary angle  $\alpha$ ) through a combination of two  $\pi$  rotations:

$$R_z(\alpha) = R\left(\pi, \frac{\alpha}{2}\right) R(\pi, 0). \quad (\text{A4})$$

The resulting  $R_z$  produces a *physical* rotation of the qubit. This fact is important, because the agnostic-sensing protocol relies on the accumulation of a physical phase difference between two qubits' states. Combining Eqs. (A2) and (A4), we implement the arbitrary rotation through

$$U(\theta_U, \phi_U, \lambda_U) = R\left(\frac{\pi}{2}, \phi_U - \pi\right) R\left(\frac{\pi}{2}, \theta_U + \phi_U\right) R\left(\pi, \frac{1}{2}(\theta_U + \phi_U + \lambda_U)\right) R(\pi, 0). \quad (\text{A5})$$

Finally, we relate the Euler angles  $(\theta_U, \phi_U, \lambda_U)$  to the arbitrary rotation through an angle  $\alpha$ , about the axis  $\hat{n} = \sin \theta \cos \phi \hat{x} + \sin \theta \sin \phi \hat{y} + \cos \theta \hat{z}$ . Given the existence of nonunique solutions, the conversion formulae we define are

$$\begin{aligned} \theta_U &= 2 \arcsin\left(\sin \frac{\alpha}{2} \sin \theta\right), \\ \phi_U &= \arctan\left(\tan \frac{\alpha}{2} \cos \theta\right) + \phi - \frac{\pi}{2}, \quad \text{and} \\ \lambda_U &= \arctan\left(\tan \frac{\alpha}{2} \cos \theta\right) - \phi + \frac{\pi}{2}. \end{aligned} \quad (\text{A6})$$

These formulae are valid for  $-\pi \leq \alpha \leq \pi$  and  $0 \leq \theta \leq \pi$ . For the boundary case where  $\alpha = \pm\pi$ , we define

$$\begin{aligned} \theta_U &= \pi - |\pi - 2\theta|, \\ \phi_U &= \text{sgn}(\pi - 2\theta) \frac{\pi}{2} + \phi - \frac{\pi}{2}, \quad \text{and} \\ \lambda_U &= \text{sgn}(\pi - 2\theta) \frac{\pi}{2} - \phi + \frac{\pi}{2}. \end{aligned} \quad (\text{A7})$$

### 3. Parametric gates

In our setup, parametric gates have been found to achieve the highest-fidelity entangled states. To implement such a gate, we modulate the ancilla qubit's frequency at approximately half of the probe-ancilla detuning, bringing the qubits into parametric resonance [Fig. 5(b)]. When calibrated, the parametric resonance gives a probe-ancilla coupling rate of 0.954 MHz, corresponding to an  $\sqrt{i}$ SWAP-gate time of 524 ns. We have optimized over the pulse envelope, obtaining a flux-modulation pulse with a gate time of 640 ns. We further find that entangling gate's parameters drift over time. Consequently, we stabilize the gate via feedback control.

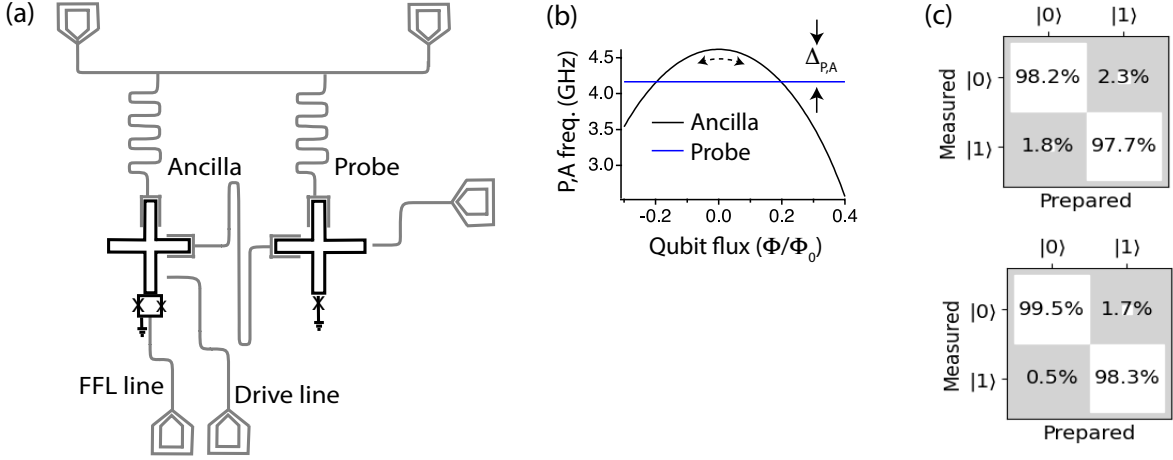


FIG. 5. **Experimental setup.** (a) The experiment involves a two-qubit section of a transmon-circuit-based processor. (b) Parametric entangling gates are activated by modulation of the ancilla frequency via the fast-flux (FFL) line. (c) Readout-fidelity matrix for the probe (top) and ancilla (bottom).

The gate’s fidelity is estimated with quantum state tomography. We measure 9 Pauli-expectation-value pairs  $\langle \Sigma_P \Sigma_A \rangle$ , with  $\Sigma_{P,A} \in \{X, Y, Z\}$ , by measuring the qubits’ reduced states simultaneously [63]. We use maximum-likelihood estimation [64] to identify the components of the probe–ancilla density matrix.

During the sensing protocol depicted in Fig. 3, we implement one  $\sqrt{i}$ SWAP gate to initialize the entangled state. Then, we projectively measure whether the system is in a singlet,  $|\Psi^-\rangle$ . That is, we measure  $\{\Pi_0, \mathbb{1} - \Pi_0\}$  (as in the main text,  $\Pi_0 := |\Psi^-\rangle\langle\Psi^-|$ ). This measurement consists of applying a second  $\sqrt{i}$ SWAP gate, which maps the singlet state to  $|e\rangle_P |g\rangle_A$ . Because the qubits have different energies, they accumulate different dynamical phases between the two  $\sqrt{i}$ SWAP gates. To remove this phase difference, we apply an additional physical rotation to the ancilla before the second  $\sqrt{i}$ SWAP gate. We implement this phase correction with the physical rotation (A4) described above.

#### 4. Effect of the parametric gate’s fidelity on the QFI measurement

As discussed in Sec. A3, we use a  $\sqrt{i}$ SWAP gate to prepare and measure the singlet. We use quantum state tomography to determine the estimated density operator  $\rho_{\text{exp}}$ . We then define the fidelity to a target state  $\sigma = |\Psi^-\rangle\langle\Psi^-|$  as [65]

$$\mathcal{F} = \left( \text{tr} \sqrt{\sqrt{\rho} \sigma \sqrt{\rho}} \right)^2. \quad (\text{A8})$$

Experimentally, we obtain  $\mathcal{F} = 0.94(.02)$ . To model the finite fidelity’s effect on the measurement, we model the experimentally realized state as

$$\rho_{\text{exp}} = \mathcal{F} |\Psi^-\rangle\langle\Psi^-| + \frac{1}{3}(1 - \mathcal{F})(\mathbb{1} - |\Psi^-\rangle\langle\Psi^-|). \quad (\text{A9})$$

This is a mixture of the target state and a maximally mixed state. The partial mixing reduces both the QFI that can be obtained and FI that we measure. From Eq. (A9), we can calculate the FI about  $\alpha$  by rotating the state, measuring the whether the system is in a singlet, repeating this process many times, and inferring the possible outcomes’ probabilities. The resulting FI is

$$I_\alpha = - \frac{(1 - 4\mathcal{F})^2 \sin^2(\alpha)}{[-5 + 2\mathcal{F} + (-1 + 4\mathcal{F}) \cos(\alpha)][1 + 2\mathcal{F} + (-1 + 4\mathcal{F}) \cos(\alpha)]}. \quad (\text{A10})$$

Figure 6 displays the  $I_\alpha$ , calculated via Eq. (A10), versus  $\alpha$ . We note two important trends. First, the FI now depends on  $\alpha$ , indicating that the singlet–triplet measurement’s metrological performance depends on the rotation’s magnitude. Second, the imperfect singlet-preparation fidelity crucially limits the advantage of manipulating entanglement to perform rotation-axis-agnostic sensing. A general analysis of the limits on the FI, in the presence of finite-fidelity operations, will be an intriguing and important direction for future research.

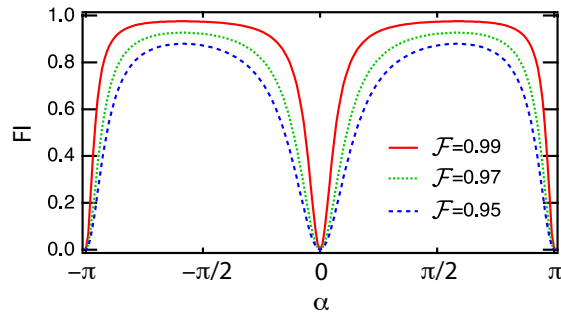


FIG. 6. FI of the agnostic-sensing protocol versus singlet-preparation fidelity.

Resource	QFI, $\mathcal{I}_\alpha$
Qubit probe	–
Qubit probe & classical ancilla	2/3
Qubit probe & entangled ancilla	1

TABLE II. Summary of theoretical results.

## B. THEORETICAL ANALYSIS OF SENSING PROTOCOLS

Here, we discuss theoretical background for the four sensing protocols laid out in the main text. First, we review the estimation of phases from locally unbiased estimators (App. B1). In App. B2, we identify a single-qubit sensor’s limitations. A qubit has only two DOFs, whereas three DOFs specify an arbitrary rotation. Hence more than one qubit is necessary for sensing a rotation about an unknown axis. In App. B3, we detail the entanglement-free sensor whose qubit probe is tagged by an ancilla. A similar strategy underlies quantum process tomography [12–15]. This sensor’s QFI is 2/3, we show. In App. B5, we prove that the qubit probe entangled with an ancilla achieves the maximum QFI over input states, 1. Table II summarizes (i) the resources required by each sensing strategy and (ii) the strategy’s effectiveness, as quantified by the QFI.

### 1. Summary of local estimation theory

A typical quantum estimation problem is structured as follows.  $M$  continuous parameters  $\boldsymbol{\alpha} := (\alpha_1, \alpha_2, \dots, \alpha_M)$  are encoded in a parameterized quantum state  $\rho_{\boldsymbol{\alpha}}$ . The goal is to infer the parameters’ values. This parameter-estimation problem is addressed within the field of quantum estimation theory. We focus on the well-established subfield of local estimation, in which  $\boldsymbol{\alpha}$  is unknown but fixed [66]. One aims to minimize the estimators’ covariances, at fixed values of the parameters. A general scheme consists of three steps [67]:

1. Prepare a parameter-independent probe state  $\rho_0$ .
2. Evolve the state under a parameter-dependent unitary  $U_{\boldsymbol{\alpha}}$ :  $\rho_{\boldsymbol{\alpha}} = U_{\boldsymbol{\alpha}}\rho_0U_{\boldsymbol{\alpha}}^\dagger$ .
3. Measure the state. The most general measurement is a positive-operator-valued measure (POVM) [68]. A POVM is a set  $\{F_k\}$  of positive-semidefinite operators ( $F_k \geq 0$ ) that sum to the identity ( $\sum_k F_k = \mathbb{1}$ ). The measurement yields outcome  $k$  with a probability  $p(k|\boldsymbol{\alpha}) = \text{Tr}[F_k\rho_{\boldsymbol{\alpha}}]$ .

The probability distribution  $p(k|\boldsymbol{\alpha})$  encapsulates information about the parameters  $\alpha_j$ .

The parameters are estimated through an estimator  $\hat{\boldsymbol{\alpha}}(k) \equiv \hat{\boldsymbol{\alpha}} := (\hat{\alpha}_1, \hat{\alpha}_2, \dots, \hat{\alpha}_M)$ . Each  $\hat{\alpha}_i$  implicitly has an argument  $k$ , which we sometimes omit for conciseness. An *estimator* is a map from the space of measurement outcomes to the space of possible parameter values. We use *locally unbiased* estimators  $\hat{\boldsymbol{\alpha}}$ :

$$\sum_k [\boldsymbol{\alpha} - \hat{\boldsymbol{\alpha}}(k)] p(k|\boldsymbol{\alpha}) = 0, \quad \text{and} \quad \sum_k \hat{\alpha}_i(k) \partial_j p(k|\boldsymbol{\alpha}) = \delta_{ij}. \quad (\text{B1})$$

The indices  $i, j \in \{1, 2, \dots, M\}$ , and  $\partial_j := \partial/\partial\alpha_j$ . The constraints in Eq. (B1) ensure that the estimator tracks the parameter's true value faithfully, to first order around the point  $\boldsymbol{\alpha}$ . The second constraint excludes pathological estimators. Examples of such include estimators that return a fixed value, irrespective of the measurement outcome.

For unbiased estimators, the accuracy of  $\hat{\boldsymbol{\alpha}}$  is quantified by its covariance matrix,

$$\text{Cov}(\hat{\boldsymbol{\alpha}}) := \sum_k [\boldsymbol{\alpha} - \hat{\boldsymbol{\alpha}}(k)] [\boldsymbol{\alpha} - \hat{\boldsymbol{\alpha}}(k)]^\top p(k|\boldsymbol{\alpha}). \quad (\text{B2})$$

Using Eqs. (B1) and (B2), one can show that the covariance matrix obeys the Cramér–Rao bound [69, 70],

$$\text{Cov}(\hat{\boldsymbol{\alpha}}) \geq \frac{1}{N} I(\boldsymbol{\alpha})^{-1}. \quad (\text{B3})$$

$N$  denotes the number of measurements, and  $I(\boldsymbol{\alpha})$  denotes the *Fisher-information matrix* (FIM):

$$I(\boldsymbol{\alpha})_{i,j} := \sum_k p(k|\boldsymbol{\alpha}) [\partial_i \log p(k|\boldsymbol{\alpha})] [\partial_j \log p(k|\boldsymbol{\alpha})]. \quad (\text{B4})$$

The FIM relates how easily we can distinguish neighboring probability distributions (parameterized by close-together  $\boldsymbol{\alpha}$  values). Therefore, the FIM quantifies the information that a probability distribution encodes about the parameters  $\alpha_i$ . The choice of measurement (step 3) affects the probabilities  $p(k|\boldsymbol{\alpha})$  and hence  $I(\boldsymbol{\alpha})$ . Certain measurements maximize the amount of information extractable from the probe. For every measurement, the inverse FIM is lower-bounded by the inverse *quantum-Fisher-information matrix* (QFIM):

$$I(\boldsymbol{\alpha})^{-1} \geq \mathcal{I}(\boldsymbol{\alpha}|\rho_{\boldsymbol{\alpha}})^{-1}. \quad (\text{B5})$$

That is,  $I(\boldsymbol{\alpha})^{-1} - \mathcal{I}(\boldsymbol{\alpha}|\rho_{\boldsymbol{\alpha}})^{-1}$  is positive-semidefinite. The QFIM is defined as [71–73]

$$\mathcal{I}(\boldsymbol{\alpha}|\rho_{\boldsymbol{\alpha}})_{i,j} := \text{Tr}[\Lambda_i \partial_j \rho_{\boldsymbol{\alpha}}], \quad (\text{B6})$$

where  $\Lambda_i$  denotes the *symmetric logarithmic derivative* (SLD), defined implicitly by  $\partial_i \rho_{\boldsymbol{\alpha}} = \frac{1}{2}(\Lambda_i \rho_{\boldsymbol{\alpha}} + \rho_{\boldsymbol{\alpha}} \Lambda_i)$  [74].

By the bound (B5), the QFIM can replace the FIM in Eq. (B3). The replacement leads to the *quantum Cramér–Rao bound* (QCRB),

$$\text{Cov}(\hat{\boldsymbol{\alpha}}) \geq \frac{1}{N} \mathcal{I}(\boldsymbol{\alpha}|\rho_{\boldsymbol{\alpha}})^{-1}. \quad (\text{B7})$$

Before analyzing the QCRB in full, we impart intuition through the special case of single-parameter estimation.

Consider estimating only one parameter,  $\alpha$  ( $M = 1$ ). The matrix inequality (B7) becomes a scalar inequality. Furthermore, in the limit  $N \rightarrow \infty$ , the bound can always be saturated [71]. To elucidate the saturation, we denote by  $\Lambda_{\alpha}$  the SLD operator associated with the parameter  $\alpha$ . Consider a POVM whose elements project onto the eigenspaces of  $\Lambda_{\alpha}$ . This POVM saturates the QCRB.

Now, consider estimating multiple parameters. The matrix inequality (B7) is not generally saturable, for the following reason. An optimal measurement basis, from which to infer about  $\alpha_i$ , is the eigenbasis of  $\Lambda_i$ . This measurement basis may be far from optimal for inferring about  $\alpha_j$ . That is, parameters' SLD operators  $\Lambda_i$  might not (weakly) commute with each other. If they do not, then one cannot achieve the optimal precision for all the parameters simultaneously. [75–78].

Furthermore, the bound (B7) has another problem, even in classical estimation theory. Consider two experimental strategies specified by two distinct POVMs,  $\Pi_1$  and  $\Pi_2$ . Let  $I_1(\boldsymbol{\alpha})$  and  $I_2(\boldsymbol{\alpha})$  denote the corresponding FIMs. There can be situations in which both  $I_1(\boldsymbol{\alpha})^{-1} \not\leq I_2(\boldsymbol{\alpha})^{-1}$  and  $I_2(\boldsymbol{\alpha})^{-1} \not\leq I_1(\boldsymbol{\alpha})^{-1}$ . The covariance matrices  $\text{Cov}_1(\hat{\boldsymbol{\alpha}})$  and  $\text{Cov}_2(\hat{\boldsymbol{\alpha}})$  lack partial ordering, defined in terms of the positive-semidefinite relation. Therefore, which strategy performs best can be unclear.

To compare strategies effectively, we introduce a scalar bound, using a real, positive-semidefinite  $M \times M$  *weight matrix*  $W$ . In terms of  $W$ , the matrix bound (B7) is recast as

$$\text{Tr}[W \text{Cov}(\hat{\boldsymbol{\alpha}})] \geq \frac{1}{N} \text{Tr}[W \mathcal{I}(\boldsymbol{\alpha}|\rho_{\boldsymbol{\alpha}})^{-1}]. \quad (\text{B8})$$

We choose  $W$  in accordance with the parameter-estimation experiment's goal. In the next subsection (B2), we choose a weight matrix to use throughout the remainder of the appendix. Particular choices of  $W$  can lead to different

optimal estimation strategies [79]. For instance, let  $W = \mathbb{1}$ , and let  $\hat{\alpha}$  be an arbitrary unbiased estimator. The left-hand side of Eq. (B8) equals the sum of the mean-square errors of the parameters in  $\hat{\alpha}$ .

Inequality (B8) motivates the QFIM as a useful performance metric in multiparameter metrology. However, Ineq. (B8) is not generally saturable. However, in the asymptotic limit of many measurements (as  $N \rightarrow \infty$ ) [78],

$$\frac{1}{N} \text{Tr}[W\mathcal{I}(\alpha|\rho_\alpha)^{-1}] \leq \text{Tr}[W\text{Cov}(\hat{\alpha})] \leq 2 \frac{1}{N} \text{Tr}[W\mathcal{I}(\alpha|\rho_\alpha)^{-1}]. \quad (\text{B9})$$

The QFIM bounds the covariance to within a factor of 2.

Often, one repeats the protocol  $N > 1$  times, using identical copies of the state  $\rho_0$ . One measures  $\rho_\alpha^{\otimes N}$ . The QFIM turns out to be additive,  $\mathcal{I}(\alpha|\rho_\alpha^{\otimes N}) = N \mathcal{I}(\alpha|\rho_\alpha)$ , implying that

$$\text{Tr}[W\text{Cov}(\hat{\alpha})] \geq \text{Tr}[W\mathcal{I}(\alpha|\rho_\alpha^{\otimes N})^{-1}] = \frac{1}{N} \text{Tr}[W\mathcal{I}(\alpha|\rho_\alpha)^{-1}]. \quad (\text{B10})$$

Hence, one can decrease the estimator's variance in two ways: first, one can increase the number  $N$  of measurements. Second, one can design a setup that reduces  $\text{Tr}[W\mathcal{I}(\alpha|\rho_\alpha)^{-1}]$ .

Finally, one can optimize the  $\rho_0$  in step 1. The QFIM  $\mathcal{I}(\alpha|\rho_\alpha)$  is convex [80]. Therefore, pure probe states achieve the maximum QFIM [81, 82].

## 2. Agnostic phase estimation

In the experiments described in the main text, the probe undergoes an arbitrary unknown rotation, represented by  $U_\alpha = \exp(-i\alpha\hat{n} \cdot \boldsymbol{\sigma}/2)$ . The unknown rotation angle is  $\alpha$ ,  $\hat{n} = \sin\theta \cos\phi \hat{x} + \sin\theta \sin\phi \hat{y} + \cos\theta \hat{z}$  defines the unknown rotation axis, and  $\boldsymbol{\sigma} = (X, Y, Z)$  denotes a vector of Pauli operators. The number of unknown parameters is  $M = 3$ . One unknown parameter is  $\alpha$ . The other two,  $\theta$  and  $\phi$ , parameterize  $\hat{n}$ . In the rest of this appendix, we will denote by  $\boldsymbol{\alpha} := (\alpha, \theta, \phi)$  the parameters to be estimated.

We aim to calculate the precision with which  $\alpha$  can be estimated. We do not aim to estimate  $\theta$  and  $\phi$ . Hence, we set the weight matrix to

$$W = \begin{pmatrix} 1 & 0 & 0 \\ 0 & 0 & 0 \\ 0 & 0 & 0 \end{pmatrix}. \quad (\text{B11})$$

The scalar bound (B10) becomes

$$\text{Var}(\hat{\alpha}) \geq \frac{1}{N} \mathcal{I}(\alpha|\rho_\alpha)^{-1}_{1,1}. \quad (\text{B12})$$

Due to the form of  $W$ , if the QFIM takes the form

$$\mathcal{I}(\alpha|\rho_\alpha) = \begin{pmatrix} \mathcal{I}_\alpha & 0 & 0 \\ 0 & \star & \star \\ 0 & \star & \star \end{pmatrix} \text{ for all } \boldsymbol{\alpha}, \quad (\text{B13})$$

then the variance  $\text{Var}(\hat{\alpha}) \geq 1/(N\mathcal{I}_\alpha)$ , irrespectively of the lower right-hand  $2 \times 2$  block  $\mathcal{I}(\alpha|\rho_\alpha)$ . (Multiplication by  $W$  always maps this block's inverse to zero.) We denote the QFI of  $\alpha$  by  $\mathcal{I}_\alpha$ , to distinguish it from the QFIM,  $\mathcal{I}(\alpha|\rho_\alpha)$ . When the QFIM is singular and not in the form (B13), one cannot estimate  $\alpha$  without knowledge of  $\hat{n}$ .

In the next section, we will see that, for every pure initial state, the single-qubit-probe protocol leads to a singular  $\mathcal{I}(\alpha|\rho_\alpha)$ , which does not decompose in the form (B13). Therefore, this protocol cannot produce any estimate of  $\alpha$ . In contrast, we show, ancilla-assisted entanglement-free sensing and entangled-sensor sensing lead to QFIMs of the desired form (B13). The QFIs for  $\alpha$  are  $2/3$  and  $1$ , respectively. Hence entanglement can boost the QFI of  $\alpha$  by 50 %.

## 3. Single-qubit sensor initiated in a pure state

We first address a particular pure state, then generalize. Consider preparing a single-qubit probe in  $|\psi_0\rangle = |0\rangle$ , the eigenvalue-1 eigenstate of  $Z$ . The probe undergoes an arbitrary unknown rotation, represented by  $U_\alpha =$



$\exp(-i\alpha\hat{\mathbf{n}} \cdot \boldsymbol{\sigma}/2)$ , as detailed in the previous subsection. The state  $|\psi_\alpha\rangle = U_\alpha|0\rangle$  achieves the QFIM

$$\begin{pmatrix} \sin^2(\theta) & -2\cos(\theta)\sin^2(\theta)\sin^2\left(\frac{\alpha}{2}\right) & \sin(\alpha)\cos(\theta)\sin(\theta) \\ -2\cos(\theta)\sin^2(\theta)\sin^2\left(\frac{\alpha}{2}\right) & 4\sin^2(\theta)\sin^2\left(\frac{\alpha}{2}\right)\left(1-\sin^2(\theta)\sin^2\left(\frac{\alpha}{2}\right)\right) & 2\sin^3(\theta)\sin^2\left(\frac{\alpha}{2}\right)\sin(\alpha) \\ \sin(\alpha)\cos(\theta)\sin(\theta) & 2\sin^3(\theta)\sin^2\left(\frac{\alpha}{2}\right)\sin(\alpha) & 4\sin^2\left(\frac{\alpha}{2}\right)\left(\cos^2(\theta)+\sin^2(\theta)\sin^2\left(\frac{\alpha}{2}\right)\right) \end{pmatrix}. \quad (\text{B14})$$

This matrix's determinant is always zero; the matrix is not invertible. Indeed, the first line of Eq. (B14) is a linear combination of the second and third lines. We can check this fact by adding the second line, multiplied by  $-\frac{1}{2}\sec\theta$ , to the third line, multiplied by  $\frac{1}{2}\cot(\alpha/2)\tan\theta$ . Furthermore, for most  $\alpha$  values, the QFIM does not satisfy Eq. (B13).

Similarly, we can calculate the QFIM for any other pure input state  $|\psi_0\rangle = a|0\rangle + b|1\rangle$ , with  $a, b \in \mathcal{C}$  and  $|a|^2 + |b|^2 = 1$ . The evolved state is  $|\psi_\alpha\rangle = U_\alpha|\psi_0\rangle$ . The corresponding QFIM is not invertible, and there are values of  $\alpha$  for which the QFIM does not satisfy Eq. (B13). We conclude that  $\alpha$  cannot be estimated from a qubit probe initiated in any pure state.

We can understand this conclusion intuitively through an example. Consider aiming to measure the strength of a magnetic field  $\mathbf{B}$  whose magnitude and direction are unknown. Suppose that we employ three (non-coplanar) detectors, each measuring the field component that points along some axis (e.g.,  $B_x$ ,  $B_y$ , or  $B_z$ ). The magnitude of  $\mathbf{B}$  (or  $\alpha$ , in our case) follows from  $|\mathbf{B}| = \sqrt{B_x^2 + B_y^2 + B_z^2}$ . The field's direction (or  $\hat{\mathbf{n}}$ , in our case) follows from  $\cos\phi = B_x/\sqrt{B_x^2 + B_y^2}$  and  $\cos\theta = B_z/|\mathbf{B}|$ . Three parameters specify the field, so one cannot measure the field's magnitude and direction using only one detector (or, in our case, a qubit probe in a pure state).

#### 4. Ancilla-assisted entanglement-free sensing

We can enhance the pure-state single-qubit probe (App. B3) even without introducing entanglement. Before showing how to do so, we elucidate a subtlety of the term *single-qubit probe*. Each of our sensing strategies requires many identical trials. Hence even the single-qubit-probe strategy (App. B3) requires many qubit probes. However, those qubits are prepared and used independently of each other.

This subsection likewise concerns a sensing strategy that involves many identical trials. In each trial, a single-qubit probe is prepared in a pure state  $|\psi_j\rangle$  selected randomly according to a probability distribution  $\{p_j\}$ . An ancilla in the state  $|j\rangle$  records which  $|\psi_j\rangle$  was prepared. The ancilla may be a qubit or a classical bit. In experiments, one tends to keep a classical record of which  $|\psi_j\rangle$  was prepared. The probe and ancilla begin in the mixture

$$\rho_0 = \sum_j p_j |\psi_j\rangle\langle\psi_j| \otimes |j\rangle\langle j|, \text{ wherein } \sum_j p_j = 1. \quad (\text{B15})$$

Suppose that one lacks knowledge of  $\alpha$  and  $\hat{\mathbf{n}}$ . The prior distribution most reasonably attributable to  $\hat{\mathbf{n}}$  is uniform. We define an *optimal* entanglement-free input state as a state that achieves the first two equalities in Eq. (2), on average with respect to the uniform distribution over  $\hat{\mathbf{n}}$ . We will show that the optimal input states have the form

$$\rho_0 = \frac{1}{3} \left( |z\pm\rangle\langle z\pm| \otimes |0\rangle\langle 0| + e^{i\phi_x} |x\pm\rangle\langle x\pm| \otimes |1\rangle\langle 1| + e^{i\phi_y} |y\pm\rangle\langle y\pm| \otimes |2\rangle\langle 2| \right). \quad (\text{B16})$$

The bases  $\{|x\pm\rangle\}$ ,  $\{|y\pm\rangle\}$ , and  $\{|z\pm\rangle\}$  (as defined in the main text) are *mutually unbiased*: for every  $a, b \in \{x, y, z\}$  such that  $a \neq b$ ,  $|\langle a\pm|b\pm\rangle| = |\langle a\pm|b\mp\rangle| = 1/\sqrt{d}$ , wherein  $d = 2$  denotes the Hilbert space's dimensionality.  $\rho_0$  is a 1 : 1 : 1 mixture of elements of three mutually maximally incompatible bases. The relative phases  $e^{i\phi_x}$  and  $e^{i\phi_y}$  are arbitrary.

In the experimental implementation, we program three different pulse sequences. Each sequence prepares one pure state ( $|x\pm\rangle$ ,  $|y\pm\rangle$ , or  $|z\pm\rangle$ ), applies the unknown unitary, and then measures the probe in a chosen basis. For each sequence, a register stores the ancilla label (effectively, 0, 1, or 2), which we use to determine which measurement (mentioned above) to perform. We perform enough experimental trials to reduce the binomial errors in our estimates of the measurement outcomes' probabilities.

Now, we show that the family of states (B16) is optimal. First, we bound the best precision attainable with any state of the form (B15), averaged over all directions  $\hat{\mathbf{n}}$ . Next, we show that the state (B16) saturates this bound. This state leads to a QFIM of the form (B13), with a QFI for  $\alpha$  of  $\mathcal{I}_\alpha = 2/3$ . Recall that the entanglement-assisted-sensing strategy (discussed in the main text) leads to  $\mathcal{I}_\alpha = 1$ . The entanglement-assisted strategy therefore performs 50 % better than the best entanglement-free strategy.

*i. Bound on the best precision attainable with ancilla-assisted entanglement-free sensing*

In this section, we bound the best precision attainable without entanglement. Equation (B15) specifies the input state. The unitary  $U_\alpha = \exp(-i\alpha\hat{\mathbf{n}} \cdot \boldsymbol{\sigma}/2)$  evolves the probe state to

$$\rho_\alpha = \sum_j p_j U_\alpha |\psi_j\rangle\langle\psi_j| U_\alpha^\dagger \otimes |j\rangle\langle j| \equiv \sum_j p_j \rho_\alpha^{(j)} \otimes |j\rangle\langle j|, \quad (\text{B17})$$

where  $\rho_\alpha^{(j)} := U_\alpha |\psi_j\rangle\langle\psi_j| U_\alpha^\dagger$ . We calculate the QFIM achievable with  $\rho_\alpha$ , using the (extended) convexity bound on the QFIM [83],

$$\mathcal{I}(\alpha|\rho_\alpha) \leq I(\alpha|\{p_j\}) + \sum_{j=1}^N p_j \mathcal{I}(\alpha|\rho_\alpha^{(j)} \otimes |j\rangle\langle j|). \quad (\text{B18})$$

$I(\alpha|\{p_j\})$  denotes the FIM, which describes the information accessible via sampling from the probability distribution  $\{p_j\}$ . In this case, the convexity bound is saturated [84]. The reason is that the states  $\rho_\alpha^{(j)} \otimes |j\rangle\langle j|$  are mutually orthogonal.

$$\mathcal{I}(\alpha|\rho_\alpha) = I(\alpha|\{p_j\}) + \sum_{j=1}^N p_j \mathcal{I}(\alpha|\rho_\alpha^{(j)} \otimes |j\rangle\langle j|). \quad (\text{B19})$$

The probabilities  $p_j$  depend on neither  $\alpha$  nor  $\hat{\mathbf{n}}$ . The first term therefore vanishes:  $I(\alpha|\{p_j\}) = 0$ . Furthermore, the QFIM is additive, since the ancilla state  $|j\rangle\langle j|$  is parameter-independent:  $\mathcal{I}(\alpha|\rho_\alpha^{(j)} \otimes |j\rangle\langle j|) = \mathcal{I}(\alpha|\rho_\alpha^{(j)}) + \mathcal{I}(\alpha||j\rangle\langle j|) = \mathcal{I}(\alpha|\rho_\alpha^{(j)})$ . Therefore,

$$\mathcal{I}(\alpha|\rho_\alpha) = \sum_{j=1}^N p_j \mathcal{I}(\alpha|\rho_\alpha^{(j)}). \quad (\text{B20})$$

Recall that we aim to lower-bound the variance of  $\alpha$ , using Eq. (B12). We need the (1, 1) component of the inverse QFIM,  $\mathcal{I}(\alpha|\rho_\alpha)^{-1}_{1,1}$ . In App. B 3, we showed that the matrices  $\mathcal{I}(\alpha|\rho_\alpha)$  are neither invertible nor generally diagonal. Therefore, calculating the inverse QFIM,  $\mathcal{I}(\alpha|\rho_\alpha)^{-1}$ , is nontrivial. Instead, we provide a method for lower-bounding  $\mathcal{I}(\alpha|\rho_\alpha)^{-1}_{1,1}$ .

The method begins with the following expression for the  $3 \times 3$  QFIM for  $\alpha$ :

$$\mathcal{I}(\alpha|\rho_\alpha) = \begin{pmatrix} \mathcal{I}_\alpha & \mathcal{I}_c^T \\ \mathcal{I}_c & \mathcal{I}_{\hat{\mathbf{n}}} \end{pmatrix}. \quad (\text{B21})$$

$\mathcal{I}_c$  denotes a two-column vector that quantifies correlations between  $\alpha$  and  $\hat{\mathbf{n}}$ .  $\mathcal{I}_{\hat{\mathbf{n}}}$  is a  $2 \times 2$  matrix that quantifies the information about  $\hat{\mathbf{n}}$ . If  $\mathcal{I}(\alpha|\rho_\alpha)$  is invertible, one can represent its inverse using the Schur complement [85]:

$$\mathcal{I}(\alpha|\rho_\alpha)^{-1} = \begin{pmatrix} \frac{1}{\mathcal{I}_\alpha - \mathcal{I}_c^T \mathcal{I}_{\hat{\mathbf{n}}} \mathcal{I}_c} & * \\ * & * \end{pmatrix}. \quad (\text{B22})$$

Since  $\mathcal{I}(\alpha|\rho_\alpha)$  is positive-semidefinite, also  $\mathcal{I}_{\hat{\mathbf{n}}}$  is positive-semidefinite. (A positive-semidefinite  $d \times d$  matrix  $A$  satisfies  $x^T A x \geq 0$  for all  $x$  in  $\mathbb{R}^d$ .) All the QFIM's entries are real, so the column vector  $\mathcal{I}_c$  is in  $\mathbb{R}^2$ . Hence,  $\mathcal{I}_c^T \mathcal{I}_{\hat{\mathbf{n}}} \mathcal{I}_c$  is non-negative. Therefore,

$$\mathcal{I}_\alpha \geq \mathcal{I}_\alpha - \mathcal{I}_c^T \mathcal{I}_{\hat{\mathbf{n}}} \mathcal{I}_c. \quad (\text{B23})$$

Inverting each side of the inequality yields

$$\frac{1}{\mathcal{I}_\alpha - \mathcal{I}_c^T \mathcal{I}_{\hat{\mathbf{n}}} \mathcal{I}_c} \geq \frac{1}{\mathcal{I}_\alpha} \quad \Leftrightarrow \quad \mathcal{I}(\alpha|\rho_\alpha)^{-1}_{1,1} \geq \frac{1}{\mathcal{I}(\alpha|\rho_\alpha)_{1,1}}. \quad (\text{B24})$$

By Eq. (B20), the (1, 1) matrix element  $\mathcal{I}(\alpha|\rho_\alpha)_{1,1}$  equals a weighted sum of the elements  $\mathcal{I}(\alpha|\rho_\alpha^{(j)})_{1,1}$ :  $\mathcal{I}(\alpha|\rho_\alpha)_{1,1} = \sum_j p_j \mathcal{I}(\alpha|\rho_\alpha^{(j)})_{1,1}$ . Recall that the prior distribution most reasonably attributable to  $\hat{\mathbf{n}}$  is uniform. We must average

over this distribution to evaluate the expected performance of our estimate of  $\alpha$ . We can substitute into the right-hand side of Ineq. (B24), if  $\mathcal{I}(\alpha|\rho)$  is invertible:

$$\text{Avg}_{\hat{\mathbf{n}}} [\mathcal{I}(\alpha|\rho_\alpha)^{-1}]_{1,1} \geq \frac{1}{\sum_j p_j \text{Avg}_{\hat{\mathbf{n}}} [\mathcal{I}(\alpha|\rho_\alpha^{(j)})]_{1,1}} = \frac{1}{2/3 \sum_j p_j} = \frac{3}{2}. \quad (\text{B25})$$

$\text{Avg}_{\hat{\mathbf{n}}}$  denotes the average with respect to a uniform distribution over the axes  $\hat{\mathbf{n}}$ . The first equality follows from a fact proved in the next subsection: consider preparing an arbitrary single-qubit pure state. It achieves a QFI that, averaged over all  $\hat{\mathbf{n}}$ , is  $2/3$ . That is,  $\text{Avg}_{\hat{\mathbf{n}}} [\mathcal{I}(\alpha|\rho_\alpha^{(j)})]_{1,1} = 2/3$ .

According to the argument above, every ancilla-assisted entanglement-free input state  $\rho_0$  leads to an average-over- $\hat{\mathbf{n}}$  quantum Fisher information  $\mathcal{I}_\alpha = 2/3$ . For such an input to be optimal, it must achieve the first two equalities in Eq. (2).  $\rho_0$  achieves this condition only if the estimation of  $\alpha$  is independent of the estimation of  $\hat{\mathbf{n}}$ . As discussed in Sec. B 4 i, this happens if and only if  $\mathcal{I}_{\hat{\mathbf{n}}} = 0$ . When  $\mathcal{I}_{\hat{\mathbf{n}}} = 0$ , Ineq. (B23) is saturated, and hence the bound (B25) is achieved. We therefore reach a necessary criterion for an entanglement-free input state to be optimal: the state must entail a QFIM of the form (B13).

In Sec. B 4 iii, we derive the optimal input states' form. We prove these states' optimality by computing the QFIM of a general one of these states. We calculate the QFIM using a convexity bound on the QFIM and exploiting the fact that the convexity bound is saturated in this case [84].

*ii. Average quantum Fisher information achievable with arbitrary pure single-qubit state*

We now prove that, for every pure single-qubit state, averaging the QFI of  $\alpha$  over all  $\hat{\mathbf{n}}$  yields  $2/3$ . Our proof strategy is direct calculation. First, we recall the forms of  $\hat{\mathbf{n}}$ ,  $A$  and  $U_\alpha$  in terms of the parameters  $\alpha$ ,  $\theta$ , and  $\phi$ . Then, we calculate the most general evolved state  $|\psi_\alpha\rangle$  and its derivative  $\partial_\alpha |\psi_\alpha\rangle$ . We substitute into a formula for the QFI, then average over  $\hat{\mathbf{n}}$ .

We have expressed the rotation axis as  $\hat{\mathbf{n}} = (\cos \phi \sin \theta, \sin \phi \sin \theta, \cos \theta)$ . In terms of this notation, the  $U_\alpha$  generator  $A = -\hat{\mathbf{n}} \cdot \boldsymbol{\sigma}/2$  has the form

$$A = \frac{1}{4} \begin{pmatrix} -\cos(\theta) & -e^{-i\phi} \sin(\theta) \\ -e^{i\phi} \sin(\theta) & \cos(\theta) \end{pmatrix}. \quad (\text{B26})$$

Hence the unitary  $U_\alpha = e^{i\alpha A}$  has the form

$$U_\alpha = \begin{pmatrix} \cos\left(\frac{\alpha}{2}\right) - i \cos(\theta) \sin\left(\frac{\alpha}{2}\right) & -ie^{-i\phi} \sin\left(\frac{\alpha}{2}\right) \sin(\theta) \\ -ie^{i\phi} \sin\left(\frac{\alpha}{2}\right) \sin(\theta) & \cos\left(\frac{\alpha}{2}\right) + i \cos(\theta) \sin\left(\frac{\alpha}{2}\right) \end{pmatrix}. \quad (\text{B27})$$

The most general input state has the form  $|\psi_0\rangle = a|z+\rangle + b|z-\rangle$ , with  $a, b \in \mathbb{C}$  and  $|a|^2 + |b|^2 = 1$ . From this expression and the previous paragraph, we can calculate  $|\psi_\alpha\rangle = U_\alpha |\psi_0\rangle$  and its derivative,  $\partial_\alpha |\psi_\alpha\rangle$ . We substitute into the QFI formula  $\mathcal{I}_\alpha = 4 \text{Re}\left\{\langle \partial_\alpha \psi_\alpha | \partial_\alpha \psi_\alpha \rangle - |\langle \partial_\alpha \psi_\alpha | \psi_\alpha \rangle|^2\right\}$  [Eq. (1) in the main text]:

$$\mathcal{I}_\alpha = \frac{1}{2} \left\{ 1 + 2|b|^2 - 2|b|^4 + (-1 + 6|b|^2 - 6|b|^4) \cos(2\theta) + 4b \left[ b(-1 + |b|^2) \cos(2\phi) \sin^2(\alpha) + a(-1 + 2|b|^2) \cos(\phi) \sin(2\theta) \right] \right\}. \quad (\text{B28})$$

Next, we average  $\phi$  and  $\theta$  over their values on the unit sphere:

$$\text{Avg}_{\hat{\mathbf{n}}} (\mathcal{I}_\alpha) = \frac{1}{4\pi} \int_0^{2\pi} \int_0^\pi \mathcal{I}_\alpha \sin \theta d\theta d\phi = \frac{2}{3}. \quad (\text{B29})$$

*iii. The optimal ancilla-assisted entanglement-free input state saturates the lower bound in Eq. (B25)*

The optimal family of ancilla-assisted entanglement-free sensors has the form

$$\rho_0 = \frac{1}{3} \left( |z\pm\rangle\langle z\pm| \otimes |0\rangle\langle 0| + e^{i\phi_x} |x\pm\rangle\langle x, \pm| \otimes |1\rangle\langle 1| + e^{i\phi_y} |y\pm\rangle\langle y\pm| \otimes |2\rangle\langle 2| \right). \quad (\text{B30})$$

As noted above,  $\rho_0$  is a 1 : 1 : 1 mixture of elements of three mutually maximally incompatible bases. The relative phases  $e^{i\phi_x}$  and  $e^{i\phi_y}$  are arbitrary.

Using Eq. (B30), we can write down different optimal input states: first, for each of  $X$ ,  $Y$  and  $Z$ , we can choose the eigenstate corresponding to the positive or negative eigenvalue. For example,  $|z+\rangle\langle z+|$  and  $|z-\rangle\langle z-|$  work equally well. Second, the arbitrary phase factors  $e^{i\phi_x}$  and  $e^{i\phi_y}$  do not affect the QFIM. One such optimal input state is

$$\rho_0 = \frac{1}{3} (|z+\rangle\langle z+| \otimes |0\rangle\langle 0| + |x+\rangle\langle x+| \otimes |1\rangle\langle 1| + |y+\rangle\langle y+| \otimes |2\rangle\langle 2|). \quad (\text{B31})$$

By Eq. (B20), the corresponding QFIM is

$$\mathcal{I}(\alpha|\rho_\alpha) = \frac{1}{3} (\mathcal{I}_{|z+\rangle} + \mathcal{I}_{|x+\rangle} + \mathcal{I}_{|y+\rangle}). \quad (\text{B32})$$

$\mathcal{I}_{|\hat{n},+\rangle}$  denotes the QFIM achievable with an input state equal to the eigenvalue-1 eigenstate of  $\hat{n}$ . Calculating the expressions for  $\mathcal{I}_{|z+\rangle}$ ,  $\mathcal{I}_{|x+\rangle}$ , and  $\mathcal{I}_{|y+\rangle}$ , we calculate the QFIM:

$$\mathcal{I}(\alpha|\rho_\alpha) = \begin{pmatrix} \frac{2}{3} & 0 & 0 \\ 0 & \frac{8}{3} \sin^2(\theta) \sin^2\left(\frac{\alpha}{2}\right) & 0 \\ 0 & 0 & \frac{8}{3} \sin^2\left(\frac{\alpha}{2}\right) \end{pmatrix}. \quad (\text{B33})$$

This QFIM's inverse is

$$\mathcal{I}(\alpha|\rho_\alpha)^{-1} = \begin{pmatrix} \frac{3}{2} & 0 & 0 \\ 0 & \frac{3}{8} \csc^2(\theta) \csc^2\left(\frac{\alpha}{2}\right) & 0 \\ 0 & 0 & \frac{3}{8} \csc^2\left(\frac{\alpha}{2}\right) \end{pmatrix}. \quad (\text{B34})$$

The (1, 1) entry equals 3/2, the lower bound presented in Ineq. (B25). Saturating this bound, the state (B31) is an optimal entanglement-free probe.

## 5. Entanglement-assisting sensing inspired by closed time-like curves

As before, we consider a probe undergoing an unknown rotation described by the operator  $U_\alpha = \exp(-i\alpha\hat{n} \cdot \boldsymbol{\sigma}/2)$ . The rotation angle is  $\alpha$ ,  $\hat{n} = \sin\theta \cos\phi \hat{x} + \sin\theta \sin\phi \hat{y} + \cos\theta \hat{z}$  defines the rotational axis, and  $\boldsymbol{\sigma} = (X, Y, Z)$  denotes a vector of Pauli operators. Relative to the  $Z$  eigenbasis, the eigenstates of  $A = -\hat{n} \cdot \boldsymbol{\sigma}/2$  are

$$|a_+\rangle = \frac{1}{\sqrt{1 + \tan^2 \frac{\theta}{2}}} \begin{pmatrix} -e^{-i\phi} \tan \frac{\theta}{2} \\ 1 \end{pmatrix} \quad \text{and} \quad |a_-\rangle = \frac{1}{\sqrt{1 + \cot^2 \frac{\theta}{2}}} \begin{pmatrix} e^{-i\phi} \cot \frac{\theta}{2} \\ 1 \end{pmatrix}. \quad (\text{B35})$$

Hence,  $U_\alpha$  can be expressed as

$$e^{-i\alpha\sigma\cdot\hat{\mathbf{n}}/2} = e^{-i\alpha/2}|a_+\rangle\langle a_+| + e^{-i\alpha/2}|a_-\rangle\langle a_-| \quad (\text{B36})$$

$$= \frac{e^{-i\alpha/2}}{1 + \tan^2 \frac{\theta}{2}} \begin{pmatrix} -e^{-i\phi} \tan \frac{\theta}{2} & \\ & 1 \end{pmatrix} \begin{pmatrix} -e^{i\phi} \tan \frac{\theta}{2} & \\ & 1 \end{pmatrix} + \frac{e^{-i\alpha/2}}{1 + \tan^2 \frac{\theta}{2}} \begin{pmatrix} e^{-i\phi} \cot \frac{\theta}{2} & \\ & 1 \end{pmatrix} \begin{pmatrix} e^{i\phi} \cot \frac{\theta}{2} & \\ & 1 \end{pmatrix} \quad (\text{B37})$$

$$= \frac{e^{-i\alpha/2}}{1 + \tan^2 \frac{\theta}{2}} \begin{pmatrix} \tan^2 \frac{\theta}{2} & -e^{-i\phi} \tan \frac{\theta}{2} \\ -e^{i\phi} \tan \frac{\theta}{2} & 1 \end{pmatrix} + \frac{e^{-i\alpha/2}}{1 + \tan^2 \frac{\theta}{2}} \begin{pmatrix} \cot^2 \frac{\theta}{2} & e^{-i\phi} \cot \frac{\theta}{2} \\ e^{i\phi} \cot \frac{\theta}{2} & 1 \end{pmatrix} \quad (\text{B38})$$

$$= e^{-i\alpha/2} \begin{pmatrix} \sin^2 \frac{\theta}{2} & -\frac{1}{2}e^{-i\phi} \sin \theta \\ -\frac{1}{2}e^{i\phi} \sin \theta & \cos^2 \frac{\theta}{2} \end{pmatrix} + e^{i\alpha/2} \begin{pmatrix} \cos^2 \frac{\theta}{2} & \frac{1}{2}e^{-i\phi} \sin \theta \\ \frac{1}{2}e^{i\phi} \sin \theta & \sin^2 \frac{\theta}{2} \end{pmatrix} \quad (\text{B39})$$

$$= \begin{pmatrix} e^{-i\alpha/2} \sin^2 \frac{\theta}{2} + e^{i\alpha/2} \cos^2 \frac{\theta}{2} & i \sin \theta \sin \frac{\theta}{2} e^{-i\phi} \\ i \sin \theta \sin \frac{\theta}{2} e^{i\phi} & e^{i\alpha/2} \sin^2 \frac{\theta}{2} + e^{-i\alpha/2} \cos^2 \frac{\theta}{2} \end{pmatrix} \quad (\text{B40})$$

$$\equiv \begin{pmatrix} a & b^* \\ b & a^* \end{pmatrix}. \quad (\text{B41})$$

The final equation defines  $a$  and  $b$  implicitly. The evolution of the probe and ancilla acts on their joint Hilbert space as

$$e^{-i\alpha\hat{\mathbf{n}}\cdot\sigma/2} \otimes \hat{\mathbb{1}} = \begin{pmatrix} a & 0 & b^* & 0 \\ 0 & a & 0 & b^* \\ b & 0 & a^* & 0 \\ 0 & b & 0 & a^* \end{pmatrix}. \quad (\text{B42})$$

Suppose that the probe and ancilla are prepared in an arbitrary Bell state  $|\mathbb{B}\rangle$ . Define the projector  $\hat{\Pi}_{\mathbb{B}} := |\mathbb{B}\rangle\langle\mathbb{B}|$ . Recall that we aim to infer  $\alpha$ . An optimal measurement is entangling and has the form  $\{\hat{\Pi}_{\mathbb{B}}, \hat{\mathbb{1}} - \hat{\Pi}_{\mathbb{B}}\}$ .

For instance, suppose that the probe and ancilla begin in  $|\Phi^+\rangle$ . If  $\hat{\Pi}_{\Phi^+} := |\Phi^+\rangle\langle\Phi^+|$ , the optimal measurement is  $\{\hat{\Pi}_{\Phi^+}, \hat{\mathbb{1}} - \hat{\Pi}_{\Phi^+}\}$ . The possible outcomes obtain with the probabilities

$$P_0 := |\langle\Phi^+|U|\Phi^+\rangle|^2 = \left| \frac{1}{2} \begin{pmatrix} 1 & 0 & 0 & 1 \end{pmatrix} \begin{pmatrix} a & 0 & b^* & 0 \\ 0 & a & 0 & b^* \\ b & 0 & a^* & 0 \\ 0 & b & 0 & a^* \end{pmatrix} \begin{pmatrix} 1 \\ 0 \\ 0 \\ 1 \end{pmatrix} \right|^2 = \left| \frac{a + a^*}{2} \right|^2 = \cos^2 \frac{\alpha}{2} \quad (\text{B43})$$

and  $P_1 = 1 - P_0 = \sin^2 \frac{\alpha}{2}$ . The resulting Fisher information is  $\text{FI} = 1$  and equals the maximum QFI. Regardless of the choice of  $|\mathbb{B}\rangle$ , if the measurement is optimal, the FIM assumes the form

$$I(\alpha|\rho_\alpha) = \begin{pmatrix} 1 & 0 & 0 \\ 0 & 0 & 0 \\ 0 & 0 & 0 \end{pmatrix}. \quad (\text{B44})$$

This FIM has the form in (B13), with  $\mathcal{I}_\alpha = 1$ .

The previous strategy provides no information about  $\hat{\mathbf{n}}$ :  $\mathcal{I}_{\hat{\mathbf{n}}} = 0$ . Suppose that we wish to garner information about  $\hat{\mathbf{n}}$ , while optimally measuring  $\alpha$ . Our protocol's measurement basis can be modified to achieve this goal, we now show. First, we calculate the QFIM achievable with a general initial Bell state,  $|\mathbb{B}\rangle$ . This calculation bounds the attainable precision:

$$\mathcal{I}(\alpha|\rho_\alpha) = \begin{pmatrix} 1 & 0 & 0 \\ 0 & 4 \sin^2(\alpha/2) \sin^2 \theta & 0 \\ 0 & 0 & 4 \sin^2(\alpha/2) \end{pmatrix}. \quad (\text{B45})$$

Now, we choose for the measurement basis to be  $\{|\Psi^+\rangle, |\Psi^-\rangle, |\Phi^+\rangle, |\Phi^-\rangle\}$ . We calculate the FIM for this choice. The FIM, we show, equals the QFIM in Eq. (B45). Therefore, this basis is the optimal basis for inferring about  $\alpha$ , while garnering information about  $\hat{n}$ .

Suppose that the input is the singlet state,  $|\Psi^-\rangle$ . One can perform similar calculations for input states equal to the other Bell states. The measurement's possible outcomes are obtained with probabilities

$$P_{\Psi^+} := |\langle \Psi^+ | U | \Psi^- \rangle|^2 = \cos^2(\theta) \sin^2\left(\frac{\alpha}{2}\right), \quad (\text{B46})$$

$$P_{\Psi^-} := |\langle \Psi^- | U | \Psi^- \rangle|^2 = \cos^2\left(\frac{\alpha}{2}\right), \quad (\text{B47})$$

$$P_{\Phi^+} := |\langle \Phi^+ | U | \Psi^- \rangle|^2 = \cos^2(\phi) \sin^2(\theta) \sin^2\left(\frac{\alpha}{2}\right), \quad \text{and} \quad (\text{B48})$$

$$P_{\Phi^-} := |\langle \Phi^- | U | \Psi^- \rangle|^2 = \sin^2(\phi) \sin^2(\theta) \sin^2\left(\frac{\alpha}{2}\right). \quad (\text{B49})$$

We differentiate these probabilities with respect to  $\alpha, \theta$ , and  $\phi$ . We can then calculate the FIM using the formula

$$I(\boldsymbol{\alpha})_{i,j} = \sum_{k \in \{\Phi^+, \Phi^-, \Psi^+, \Psi^-\}} \frac{(\partial_i P_k)(\partial_j P_k)}{P_k^2}. \quad (\text{B50})$$

The result is

$$I(\boldsymbol{\alpha}) = \mathcal{I}(\boldsymbol{\alpha} | \rho_{\boldsymbol{\alpha}}) = \begin{pmatrix} 1 & 0 & 0 \\ 0 & 4 \sin^2(\alpha/2) \sin^2 \theta & 0 \\ 0 & 0 & 4 \sin^2(\alpha/2) \end{pmatrix}, \quad (\text{B51})$$

which has the form of the optimal QFIM [Eq. (B45)].

---